Journal Pre-proofs

Enhanced oral permeability of *Trans*-Resveratrol using nanocochleates for boosting anticancer efficacy; *in-vitro* and *ex-vivo* appraisal

Mohamed G. El-Melegy, Hoda M. Eltaher, Ahmed Gaballah, Amal H. El-Kamel

PII: S0939-6411(21)00232-0
DOI: https://doi.org/10.1016/j.ejpb.2021.08.020
Reference: EJPB 13653

To appear in: *European Journal of Pharmaceutics and Biopharmaceutics*

Received Date: 7 July 2021
Revised Date: 13 August 2021
Accepted Date: 27 August 2021

Please cite this article as: M.G. El-Melegy, H.M. Eltaher, A. Gaballah, A.H. El-Kamel, Enhanced oral permeability of *Trans*-Resveratrol using nanocochleates for boosting anticancer efficacy; *in-vitro* and *ex-vivo* appraisal, *European Journal of Pharmaceutics and Biopharmaceutics* (2021), doi: https://doi.org/10.1016/j.ejpb.2021.08.020

Enhanced oral permeability of *Trans*-Resveratrol using nanocochleates for boosting anticancer efficacy; *in-vitro* and *ex-vivo* appraisal

Mohamed G. El-Melegy[a], *Hoda M. Eltaher*[a, *], *Ahmed Gaballah*[b] *Amal H. El-Kamel* [a]

[a] *Department of Pharmaceutics, Faculty of Pharmacy, Alexandria University, 21521, Alexandria, Egypt*
[b] *Microbiology Department, Medical Research Institute, Alexandria University, 21561, Alexandria, Egypt*

[*]Corresponding Author
Email: hoda.amin@alexpharmacy.edu.eg

The ORCID identification number for the corresponding author of this article can be found under: https://orcid.org/0000-0001-5602-2696

Abstract:

Hepatocellular carcinoma (HCC) is a prevalent liver cancer representing the fourth most lethal cancer worldwide. *Trans*-Resveratrol (T-R) possesses a promising anticancer activity against HCC. However, it suffers from poor bioavailability because of the low solubility, chemical instability, and hepatic metabolism. Herein, we developed T-R-loaded nanocochleates using a simple trapping method. Nanocarriers were optimized using a comprehensive in-vitro characterization toolset and evaluated for the anticancer activity against HepG2 cell line. T-R-loaded nanocochleates demonstrated monodispersed cylinders (163.27±2.68 nm and 0.25±0.011 PDI) and -46.6 mV ζ-potential. They exhibited a controlled biphasic pattern with minimal burst followed by sustained release for 72 h. Significant enhancements of Caco-2 transport and ex-vivo intestinal permeation over liposomes, with 1.8 and 2.1-folds respectively, were observed. Nanocochleates showed significant reduction of 24 h IC50 values compared to liposomes and free T-R. Moreover, an efficient knockdown of anti-apoptotic (Bcl-2) and cancer stemness (NANOG) genes was demonstrated. To the best of our knowledge, we are the first to develop T-R loaded nanocochleates and scrutinize its potential in suppressing NANOG expression, 2-folds lower, compared to free T-R. According to these auspicious outcomes, nanocochleates represent a promising nanoplatform to enhance T-R oral permeability and augment its anticancer efficacy in the treatment of HCC.

Keywords: Trans-Resveratrol; Nanocochleates; *Ex-vivo* Permeation; Caco-2 Permeation; Hepatocellular Carcinoma; HepG2 cells; Apoptosis; NANOG

1. Introduction

Hepatocellular carcinoma (HCC) is the fourth most common leading cause of cancer-related death worldwide [1]. It constitutes a substantial health burden as projected responsible for 90% of primary liver cancers [2]. HCC is controlled by surgical and chemotherapeutical strategies, which often cause severe adverse effects like skin, endocrine and gastrointestinal disorders [3]. Over the past decades, extensive efforts have been made to develop effective therapies with improved outcomes and minimal side effects. Several therapeutic agents have been elaborated for the management of HCC such as sorafenib, brivanib, oxaliplatin among other chemotherapeutic agents [4]. However, these traditional approaches have not been effective in diminishing the global mortality rate for patients diagnosed with HCC. Accordingly, novel therapeutic strategies are required to improve the overall survival rate.

Unlike synthetic drugs, phytopharmaceuticals have recently gained widespread attention because of their relative safety and biocompatibility. Among various phytomedicines, polyphenols are considered as an attractive alternatives to other conventional chemotherapeutic agents in cancer therapy as they exhibit reduced toxicity [5]. *Trans*-Resveratrol (3,5,4′-trihydroxystilbene; T-R), one of the most promising naturally occurring polyphenols, is commonly found in grapes, berries, red wine, peanuts and several herbs for instance Polygonum cuspidatum [6]. As a polyphenol, the structure of T-R consists of two phenolic rings (monophenol and diphenol) linked together by a styrene double bond where its isomer exists in the *trans* configuration [7]. The *trans*-isomer is more pharmacologically active than *cis*-isomer [6]. It has been shown to exhibit a broad range of beneficial therapeutic and preventive properties including antioxidant [8], anti-inflammatory [9], cardioprotective [10], anti-diabetic [11], neuroprotective [12] and anti-tumor activities [13]. Recently, T-R has shown positive anticancer effects on a wide range of solid tumor cells such as those of the breast, liver, prostate, colorectum and pancreas as well as on gliomas [13]. T-R can interrupt or avert all stages of carcinogenesis *in-vitro* and *in-vivo*, including initiation, promotion and progression [14]. Likewise, previous studies have reported that T-R inhibits cell proliferation and induces cell apoptosis in HCC [15].

The clinical applications of native T-R in the treatment of human cancers face major challenges mostly attributed to its high lipophilicity; log P 3.1 and low (~3 mg/100 mL) aqueous solubility [6]. These properties come along with T-R chemical instabilities including photo-

isomerization [16, 17], oxidation [17, 18], pH and temperature degradation [19, 20] and hepatic metabolism [6]. Altogether, they contribute progressively to poor oral bioavailability (<1%) [16]. The aforementioned challenges often result in high dosing frequency with inevitable adverse effects. Since T-R demonstrates acceptable permeability and is considered as a class II compound in the Biopharmaceutical Classification System (BCS) [6], enhancement of its aqueous solubility would serve to improve oral bioavailability by increasing the amount of drug available for absorption. To circumvent such limitations, several delivery systems have been developed for enhancing solubility, stability, bioavailability and targeting ability of T-R, such as liposomes [21], dendrimers [22], self-nano-emulsifying drug delivery systems [23], solid lipid nanoparticles [24], nanosuspensions [25], nanocapsules [26], nanoemulsion [27], nanobubbles [28], nanofibers [29], niosomes [30] and transferosomes [31].

In this framework, conventional liposomes are usefully recognized lipid-based nanocarriers nevertheless they often suffer from poor mechanical stability such as leakage and also low encapsulation efficiency of loaded drugs [32]. In accordance, the *in-vitro* stability of T-R within liposomal systems might be compromised. From these perspectives, it is imminent to develop novel and effective nanocarriers of T-R with superior encapsulation efficiency and shelf-life stability, which in turn can enhance the overall oral permeability and intensify the anticancer efficacy. Over the past few decades, nanocochleates have emerged as valuable lipid-based delivery nanoplatform for enhancing solubility and permeability of numerous highly hydrophobic drugs that were designated "challenging to deliver orally" [33]. As an example, oral formulation of amphotericin B (AmB) was often deemed challenging because of its weak solubility and permeability [34]. Interestingly, the elaboration of an oral AmB-loaded nanocochleates formulation was accomplished by BioDelivery Sciences, Inc. displaying a potent antifungal impact parallel to intravenous (IV) route [35].

Nanocochleates are stable cigar-like spiral rolls, composed of positively charged divalent calcium ions and negatively charged phospholipid [36]. The unique structure of nanocochleates is highlighted by spiral lipid sheets, in which a large, continuous and planar phospholipid bilayer sheet is coiled around an initial point of folding with little or no interior aqueous space [37]. When calcium ions bind with the anionic phospholipid head groups of one bilayer and that of the opposite bilayer, the internal aqueous core of small unilamellar vesicles (SUVs) is excluded. This results in

fusion of the lipid bilayers and construction of supramolecular self-assemblies constituted of rolled sheets. Nanocochleates can be made up of simple phospholipids mainly obtained from naturally occurring cell membranes of either animal or plant source [38]. Hence, they can be considered as non-toxic, non-immunogenic and non-inflammatory [36]. Moreover, these lipid-based self-assemblies permit prominent encapsulation of different drug categories, particularly highly hydrophobic ones [36]. In contrast to liposomes, the non-aqueous structure of nanocochleates acts as a resistant barrier to penetration by oxygen and subsequently less vulnerable to oxidation of encochleated; encapsulated drug molecules [37]. Being comprised of a series of solid rigid layers, components encochleated within the interior of nanocochleates remain relatively intact, albeit the outer layers may be exposed to harsh environmental circumstances such as sunlight, oxygen, water and temperature or even GIT enzymes [36]. In this regard, the nanotechnology of encochleation possesses a promising potential for improvement of multitude aspects of formulated product including ease of production, enhancing the formulation quality, providing sustained release of the drug, increasing processing and shelf-life stability as well as complete biodegradability and biocompatibility for systemic administration [39, 40]. With this background, we developed T-R-loaded nanocochleates to improve the physicochemical characteristics of T-R including its solubility and shelf-stability for the first time with the purpose of enhancing its oral permeation and therapeutic efficacy in management of HCC.

In this current study, T-R- loaded conventional liposomes and nanocochleates were developed and evaluated by a comprehensive toolset of *in-vitro* characterization techniques. The optimized formulations were further appraised by morphological, solid-state investigations and *in-vitro* release along with shelf-stability. The enhancement of oral permeation was realized using *in-vitro* cell culture assay and *ex-vivo* intestinal model. Furthermore, in-depth evaluation of the *in-vitro* anticancer activity was scrutinized in human liver cancer cell line in terms of cytotoxicity, cellular uptake, apoptosis and gene expression.

2. Materials and methods

2.1. Materials

Trans-Resveratrol (T-R) (purity > 98%) was purchased from (Guangzhou Phytochem Sciences Inc., Guangzhou, China). Lipoid® S75 (Fat-free soybean phospholipids with 70 % phosphatidylcholine (PC)) was a kind gift from Lipoid AG (Ludwigshafen, Germany). Cholesterol

(Ch) was purchased from Sigma-Aldrich (St. Louis, Mo, USA). Calcium chloride ($CaCl_2$) anhydrous was purchased from Oxford lab chem. (India). Dulbecco's Modified Eagle's Medium (DMEM) high glucose, heat-inactivated fetal bovine serum (FBS), streptomycin/penicillin and other cell culture materials were purchased from Lonza Verviers SPRL (Belgium). 3-(4,5-dimethylthiazol-2-yl)-2,5-diphenyltetrazolium bromide (MTT) was purchased from SERVA Electrophoresis GmbH (Germany). TRIzol® Reagent and Hoechst 33342 were purchased from Invitrogen, Thermo Fisher Scientific (Waltham, MA, USA). All the primers were purchased from Willowfort® Co. (UK). HPLC grade acetonitrile and DMSO were purchased from Fischer Scientific (Loughborough, UK). All other used chemicals, solvents and reagents were of analytical grade. Human cancer cell lines (HepG2, Caco-2) were obtained from Center of Excellence for Research in Regenerative Medicine and its Applications (CERRMA), Faculty of Medicine, Alexandria University.

2.2. High-performance liquid chromatography of T-R

A reported validated HPLC method [41] was utilized for quantification of T-R with a slight modification. The HPLC instrument (Agilent Technologies-1260 Infinity, Germany) was equipped with a UV-variable wavelength detector (G1314F) set at λ_{max} 306 nm, a reversed-phase C_{18} column (Agilent HC-C_{18} [4.6×250 mm], 5 µm particle size) and Agilent ChemStation® software 32-bit version (revision B.02.01 SR1). A degassed mixture of acetonitrile and de-ionized water (40:60 v/v) was utilized as an isocratic mobile phase. The mobile phase was run at a flow rate of 1.0 mL/min under a controlled temperature (30°C) and the injected sample volume was 20 µL. The analytical method was validated concerning linearity, specificity, precision, limits of detection and quantification, and recovery.

2.3. Determination of saturated solubility of T-R

The saturated solubility of T-R was determined in phosphate buffers; pH 6.8 and 7.4 and acetate buffer pH 5.5 at 37 ℃. Excess T-R was added to 3 mL buffer in a capped dark bottle placed in a thermostatically shaking water bath (Wise bath®, Model WSB-18, UK) equipped at 100 rpm for 24 h followed by another 24 h equilibrium. Samples from the supernatant were then filtered through 0.45µm PTFE syringe filter (Chromtech®, UK), diluted and analyzed by the HPLC method mentioned in section 2.2.

2.4. Determination of pH stability of T-R

Amounts equivalent to the saturated solubilities values of T-R in different buffer media determined in section 2.3, were placed into amber glass vials in thermostatically controlled water bath at 37 ± 0.5 ℃ under continuous shaking at 100 rpm. Samples were withdrawn at pre-determined time intervals 24, 48 and 72 h and filtered through 0.45µm PTFE syringe filter, diluted and analyzed by the HPLC method mentioned in section 2.2.

2.5. Preparation of anionic T-R-loaded liposomes

2.5.1. Thin film hydration

Conventional liposomes loaded with T-R (R-Lipo) were prepared by a previously reported thin film hydration technique [42] at dark conditions. Briefly, 70 mg of Lipoid® S75 and 30 mg of Ch were dissolved along with 5 mg of T-R in 5 mL of 100% chloroform in a round-bottomed flask by gentle swirling. The obtained organic solution was evaporated under vacuum using rotary evaporator (BÜCHI 461 Corporation, Switzerland) supplied with oil-free vacuum pump (ROCKER®, Model Rocker 801, Taiwan) to obtain a thin film. Traces of organic solvent were removed by placing the flask under vacuum for 15-20 min. The dried lipid film was then hydrated with 5 mL acetate buffer (0.1 M, pH 5.5). The dispersion was stirred for 30 min in a water bath at a constant temperature above the chain melting temperature (T_m) of lipoid S75 (40 ± 2 ℃). To obtain uniform dispersion of vesicles, the resulting liposomal suspension was further subjected to pulsed ultrasonication using SONOPULS probe sonicator (BANDELIN electronic, Germany) for 10 min (60 sec-cycle, 70% amplitude) in an ice bath. Vesicular dispersion was stored at 4 ± 0.5 °C overnight for stabilization before further characterization.

2.5.2. Ethanol injection

SUVs were prepared by a previously described ethanol injection method [43] at dark conditions. First, 70 mg of Lipoid® S75 and 30 mg of Ch were dissolved together with 5 mg of T-R in 2 mL of absolute ethanol and heated up to the phase transition temperature (40 ± 2 ℃) of Lipoid® S75. Then, the dissolved mixture was rapidly injected, through a 23G syringe, into 5 mL of acetate buffer (0.1 M, pH 5.5) under magnetic stirring (JP Selecta, Multimatic-9-N, Spain) at 1000 rpm. The system was subjected to evaporation under vacuum for 10-15 min at a temperature 40 ± 2 ℃ to remove any residual ethanol. Thereafter, it was further stirred magnetically at 1000

rpm at room temperature for 1 h. Liposomal dispersion was stored at 4 ± 0.5 °C overnight for stabilization before further characterization.

2.6. Preparation of T-R-loaded nanocochleates

Nanocochleates loaded with T-R (R-CO) were prepared according to trapping method described by Bothiraja *et al.* [44] under dark conditions. Aliquots of 300, 500, 1000 and 1750 µL of $CaCl_2$ stock solution (100 mM $CaCl_2$ in de-ionized water) were added slowly (100 µL/min) using syringe pump (Model NE-4000, KF Technology Srl, Italy) into 5 mL of the prepared R-Lipo suspensions. The process was completed under vigorous stirring at 1500 rpm for 30 min, until final $CaCl_2$ concentrations of approximately 6, 9, 16.7 and 26 mM were achieved, respectively. Finally, nanocochleates dispersions were kept in the dark at 4 ± 0.5 °C overnight for stabilization before further characterization.

Blank counterparts of liposomes and nanocochleates were prepared using the same procedures, devoid of T-R and are referred to as (B-Lipo) and (B-CO), respectively.

2.7. In-vitro characterization

2.7.1. Particle attributes (Size distribution and ζ-potential)

The prepared formulations of R-Lipo and R-CO were subjected to mean particle size (PS), polydispersity index (PDI) and ζ-potential (ZP) measurement using zeta sizer (Malvern Zetasizer® Nano ZS90, Malvern Instruments, Malvern, UK) at 25 °C and scattering angle of 173°. Formulations were diluted with filtered de-ionized water (1:200) and vortexed for 1-2 min prior to analysis.

2.7.2. Entrapment efficiency, drug loading and product yield

Entrapment efficiency was determined using ultrafiltration technique [45]. Liposomal (R-Lipo) and nanocochleates (R-CO) formulations were added to Vivaspin® centrifugal tubes (MWCO 100,000 Da, Sartorius Lab Instruments, Germany) and centrifuged using cooling centrifuge (Sigma 3–30K, Germany) at 6000 rpm for 15 min at 4 °C. The clear filtrates were then separated and analyzed by HPLC for determination of the amount of free drug. Entrapped T-R was computed by difference from the total amount of drug added. Freshly prepared vesicular and nanocochleates suspensions were centrifuged at 20,000 rpm for 30 min at 4 °C. Pellets containing

nanocarriers were resuspended in de-ionized water and freeze-dried using Cryodos-50 lyophilizer (Telstar, SA, Terrassa, Spain).

The entrapment efficiency (EE%), drug loading (DL) and overall product yield (%) were calculated as follows [46]:

$$\text{Entrapment efficiency (\%W/W)} = \frac{Amount\ of\ drug\ entr}{Total\ amount\ of\ drug\ us}$$

(Equation 1)

$$\text{Drug loading (W/W)} = \frac{Amount\ of\ drug\ entrapped\ in\ the\ nanocarriers\ (mg)}{Total\ theoretical\ \ weight\ of\ the\ nanocarriers\ (g)}$$

(Equation 2)

$$\text{Product yield (\%W/W)} = \frac{Weight\ of\ recovered\ nanocarriers\ (mg)}{Total\ theoretical\ weight\ of\ lipids + drug\ used\ (mg)} * 100$$

(Equation 3)

2.7.3. Morphological examination

2.7.3.1. Scanning electron microscopy (SEM)

The morphology of the optimized R-Lipo and R-CO formulations was investigated by scanning electron microscope (SEM, JSM-IT200; JEOL, Tokyo, Japan). A droplet of the sample suspension in de-ionized water was mounted on an aluminum stub, excess liquid was removed. Then the sample was vacuum dried and sputter-coated with gold using ion sputtering coater for 30 min prior to examination. The samples were then scanned at 20 kV acceleration voltage.

2.7.3.2. Transmission electron microscopy (TEM)

Transmission electron microscope (TEM, JEM-2100F; JEOL, Tokyo, Japan) was used to visualize the morphology of the optimized nanocarriers and to confirm the rolling structure of nanocochleates. Prior to the analysis, aqueous dispersions of freshly prepared samples were diluted with filtered de-ionized water (1:6) and subjected to bath sonication for 5 min at room temperature.

Thin film was obtained by placing a sample drop into a carbon-coated copper grid then stained with aqueous solution of 1% uranyl acetate for 30 s. A filter paper was used to remove excess staining solution and allowed to dry out. After that, the stained film was visualized under TEM operated at an accelerating voltage of 80 kV.

2.7.4. Solid-state properties

2.7.4.1. Differential scanning calorimetry (DSC)

Thermograms of T-R, freeze-dried of selected R-Lipo and R-CO in addition to their physical mixtures were recorded using DSC (PerkinElmer Inc, Shelton, CT, USA). Briefly, 5 mg of each sample was spread, sealed hermetically in an aluminum pan and heated at a constant rate of 10 ℃/min over a temperature range of 25-400 ℃.

2.7.4.2. Fourier-transform infrared spectrometry (FTIR)

FTIR analyses of T-R, PL, Ch, $CaCl_2$, the selected freeze-dried R-Lipo and R-CO as well as their respective physical mixtures, were performed using a FTIR spectrometer (PerkinElmer Inc, Shelton, CT, USA). Pellets were prepared by grinding 2 mg of samples, then mixing with 200 mg of pure potassium bromide powder that were subsequently compressed into discs. A spectrum for each sample was measured within the wave number region of 4000 – 450 cm^{-1} at room temperature.

2.7.5. In-vitro T-R release

Dialysis bag diffusion method [44] was used to study the release profile of T-R from liposomes and nanocochleates after inspecting the diffusivity of drug via dialysis membrane. Samples equivalent to 1 mg of T-R were taken from each selected formulations and free drug suspension (acetate buffer, pH 5.5). The samples were individually placed into dialysis bags (MWCO 12,000-14,000 Da, Visking®, SERVA, Germany) tied properly from both ends. After that, dialysis bags were immersed in 150 mL dissolution medium of phosphate-buffered saline (PBS, pH 6.8) which was chosen to confirm sink conditions and maintained at 100 rpm and 37 ± 0.5℃ away from direct light. Aliquots of 0.5 ml were withdrawn and replaced by fresh pre-warmed medium at predetermined time points. The concentrations of samples were analyzed by HPLC and the cumulative percent of drug released was then plotted. The mechanism of drug release from conventional liposomes and nanocochleates was investigated using various

mathematical models. Data was fit in the DDSolver, an add-in program for Microsoft Excel, for modeling and comparison of drug release profiles [47]. Cumulative percent of T-R released was calculated by dividing the amount of T-R released in the entire volume by the total amount of T-R-loaded in liposomes and nanocochleates. These values were corrected for the amount of T-R removed at each time interval [48].

2.7.6. Shelf-stability study

In order to investigate the storage stability of liposomes and nanocochleates, the selected optimized formulations were stored as lyophilized powders, without any cryoprotectant, in a desiccator containing $CaCl_2$ at 25 ± 2 ℃ (< 5% RH). Reconstitution was carried out by shaking of lyophilized samples, in the original volume of acetate buffer (pH 5.5) at room temperature until homogenously dispersed. Evaluation was conducted in terms of changes in mean PS, PDI, ZP and EE % after 1, 3 and 6 months. Furthermore, TEM images of T-R-loaded liposomes and nanocochleates were captured at the end of the study.

2.8. Permeation studies

2.8.1. In-vitro permeation

2.8.1.1. Cell culture

Caco-2 cells (colorectal adenocarcinoma cell line) were cultured in DMEM and high glucose (4.5 g/L) supplemented with 10% (v/v) FBS, 1% non-essential amino acids and 1% L-glutamine supplied with penicillin G (100 IU/mL) and streptomycin (100 µg/mL). Cells were maintained in a humidified CO_2 incubator (Thermo Fisher Scientific, Waltham, USA) with 5% CO_2 and 95% air at 37°C. For experimentation, passages 30-50 were used.

2.8.1.2. Transport across Caco-2 monolayer

Caco-2 cells were seeded on translucent PET filter inserts (ThinCert™ insert, Greiner Bio-One, Germany) of 113.1 mm^2 culture surface; 0.4 µm pore size (apical chambers) at a seeding density of approximately 10^5 cells/well. The inserts were placed onto 12-well Transwell® cell-culture plates containing 2 mL of the medium (basolateral chamber). The cells were then maintained for a period of 21-24 days before the transport study with a fresh medium replacement interval of 1–2 days. The integrity of the monolayer culture was monitored by inverted light microscopy and by the measurement of transepithelial electrical resistance (TEER) using an EndOhm tissue resistance

measurement chamber equipped with 'chopsticks' electrodes both in the beginning and at the end of experiment. Caco-2 monolayers exhibiting a TEER value of > 250 Ω.cm^2 were used within 21 days post-seeding. The transport experiments across the cell monolayers were performed from the apical to the basolateral direction in Hank's Balanced Salt Solution (HBSS) of adjusted pH 6.8 at 37 °C. Before permeation experiments, the culture medium was removed, Transwell® inserts and receiver chambers were rinsed with HBSS, preincubated in HBSS at 37 °C for 15 min in a CO_2 incubator. After that, an equivalent dose of 0.5 mg of T-R suspension (acetate buffer, pH 5.5), selected optimized formulations of R-Lipo and R-CO were pipetted into the apical side of the chambers separately. At predetermined different time intervals, 0.25, 0.5, 0.75, 1, 2, 4, 6 and 24 h, an aliquot of 0.2 mL was withdrawn from the permeated basolateral side of the chambers and replaced with an equal volume of fresh pre-warmed HBSS. At the end of the experiment, the integrity of Caco-2 monolayers was confirmed by means of Hoechst 33342 staining assay using confocal laser scanning microscope (CLSM) (Leica® Microsystems Inc. Model DMi8, Wetzlar, Germany) which was compared with the captured images of monolayers on 9th day of post-seeding. Permeated amount of the drug passed through the basolateral side was analyzed by the previously described HPLC. Experiments were conducted in triplicates. The apparent permeability coefficient (P_{app}) of T-R and the optimized formulations was then calculated by the following equation [49].

$$P_{app} = V_R * \frac{dC}{dt} * \frac{1}{A * C_0} \quad \textbf{(Equation 4)}$$

Where,

- P_{app}: Apparent permeability coefficient (cm/s)
- dc/dt: Cumulative concentration of drug (c) appearing in the basolateral chamber as a function of time (t) and was obtained from the slope of the linear portion of the concentration *vs.* time plot
- A: Surface area of the monolayer filter
- C_0: Initial concentration of drug in the apical chamber (mg/mL)
- V_R: Volume of the basolateral chamber (mL)

2.8.2. Ex-vivo intestinal permeation

Ex-vivo permeation studies of T-R and selected optimized formulations of R-Lipo and R-CO were carried out using the non-everted intestinal sac model [50]. A total of 20 male Wistar albino rats (weighing 200 ± 20 g) were used in the study. Experiments were performed according to approval and ethical guidelines of Institutional Animal Care and Use Committee (IACUC) of Alexandria University (AU 062021321196) along with the U.K. Animals (Scientific Procedures) Act, 1986 and the European Community guidelines for animal experiments (EU Directive 2010/63/EU). The rats were housed in a temperature and humidity-controlled room (23°C, 55% air humidity) with free access to water and standard rat chow. The rats were adapted for at least 5 days and fasted overnight but supplied with water ad libitum before the experiment. Animals were sacrificed by cervical dislocation and the small intestine was immediately excised after sacrifice by cutting across the upper end of the duodenum and the lower end of the ileum and manually stripping the mesentery. The small intestine was washed out carefully with cold normal oxygenated saline solution (0.9% NaCl) several times using a syringe equipped with a blunt end. The clean intestinal tract was cut into 17 ± 0.2 cm long segments having a diameter of 3.0 ± 0.5 mm.

Each sac was filled with an equivalent volume to 0.5 mg of control (T-R suspension in acetate buffer, pH 5.5), selected optimized formulations of R-Lipo and R-CO separately via a blunt needle, and the two sides of the intestine were tied securely with a thread. Each non-everted intestinal sac was soaked in a conical flask containing 25 ml of the diffusion medium (Ringer's solution, pH 6.8) to achieve sink conditions. The entire system was maintained at 37° C in a shaking water bath operated at 100 rpm and well aerated with 5% CO_2 and 95% O_2 (10–15 bubbles/min) using a laboratory aerator. Samples (1 mL) were withdrawn from outside of the sac after predetermined time intervals (0.25, 0.5, 0.75, 1, 1.5 and 2 h) and promptly compensated with an equal volume of fresh pre-warmed medium. Samples were filtered using 0.22 µm pore size PTFE syringe filters followed by analysis by the HPLC method mentioned (section 2.2). The study was performed in a triplicate. Cumulative amount of T-R permeated was plotted after correction of the amount of T-R removed at each time interval [48] and then P_{app} values of the samples were calculated according to **Eq. (4)**.

2.9. Anti-cancer activity

2.9.1. Cell Culture

HepG2 cells (Hepatocellular carcinoma cell line) were cultured in high-glucose DMEM supplemented with 10% (v/v) FBS and 2 mM L-glutamine. A total of 100 IU/mL penicillin G and 100 µg/mL streptomycin were added to the medium and cells were incubated in a humidified CO_2 incubator with 5% CO_2 at 37°C.

2.9.2. In-vitro cytotoxicity

The cytotoxic effects of T-R were evaluated using MTT assay [51]. Different micromolar concentrations of T-R solution in absolute DMSO were prepared freshly and wrapped in aluminum foil for protection against light. HepG2 cells (5×10^3 cells/well) were seeded into 96-well plates (Greiner Bio-One, Germany) and were incubated in a humidified atmosphere of 5% CO_2 at 37°C for 24 h for adhesion. After incubation, supernatant media were replaced with an equal volume of fresh media containing different concentrations (2.5, 10, 30, 50, 70, 100, 140 and 200 µM) of pure T-R or optimized formulations of R-Lipo and R-CO. After incubation for 24 and 48 h of treatments, 50 µL of MTT solution (5 mg/mL MTT in PBS) was added to each well using a multi-well pipettor and the cells were incubated for further 4 h in the dark at 37° C and 5% CO_2. After incubation, culture media were removed, and 150 µL of DMSO was added to each well followed by gentle shaking of the plates on an orbital shaker for 10 min to dissolve the formazan crystals. Cell Viability was estimated by measuring the absorbance at λ_{max} 570 nm ($A_{570\ nm}$) using an automated ELISA microplate reader (BioTek® Instruments, VT, USA).

Results were expressed as a percentage of cell viability, with 100% representing control cells treated with absolute DMSO alone. Treated and control cells were exposed to 0.3 % DMSO final concentration. All experiments were performed in triplicates. The percentage of cell viability was calculated using **Eq. (5)** where $A_{treated}$ is the mean absorbance of treated cells while $A_{control}$ is the mean absorbance of control cells. The 50% of growth inhibitory concentration (IC_{50}) was calculated from a plotted dose-response curve using the non-linear regression analysis using GraphPad Prism (version-7.04).

$$\text{Survival rate (\%)} = (A_{treated}/A_{control}) * 100 \qquad \textbf{(Equation 5)}$$

2.9.3. Cellular uptake of R-Lipo and R-CO

Inherent green fluorescence of T-R was used to visualize the uptake of drug-loaded liposomes and nanocochleates. HepG2 cells (5×10^5 cells/well) were seeded in 6-well plates containing a cover slip. The cells were incubated for 1 day and then treated with T-R/DMSO solution or selected optimized formulations of R-Lipo and R-CO equivalent to the IC_{50} (24 h treatment) of T-R in DMSO solution (section 2.9.2) and incubated for 1h at 37℃. At the end of the incubation period, the media were aspirated, and the cell wells were rinsed with PBS and fixed with 4% paraformaldehyde solution in PBS for 15 min at room temperature. The cells were then washed again with PBS, the coverslip was mounted on slides and cellular uptake was observed using Leica confocal microscope (Model DMi8) with the excitation wavelength of 355 nm. All procedures were carried out away from direct light to prevent the detrimental influence of ambient light. Confocal images were analyzed using ImageJ 1.52a software developed by National Institutes of Health, USA. For each treatment, identical fields of each image were analyzed. 3D surface plots were drawn and brightness values (arbitrary units) of all the images were measured and expressed as mean fluorescence intensity.

2.9.4. Apoptosis studies

2.9.4.1. Nuclear Staining

The nuclei of HepG2 cells were analyzed for apoptogenic activity by DNA-binding dye, Hoechst 33342 staining following the standard protocol [52]. The cells were added to 6-well plates at a cell density of 5×10^5 cells/well and then treated with each of the IC_{50} (24 h treatment) of selected optimized formulations of R-Lipo and R-CO, respectively. After 1 h of incubation, the cell wells were washed with PBS, fixed with 4% paraformaldehyde solution and then Hoechst 33342 in PBS at a final concentration of 10 µg/mL, was added. After 15–20 min of incubation at room temperature in the dark, the cells were washed again with PBS and adequate culture medium was added to cover the surface of the wells. The cells nuclei were then observed, and photographs were captured using Leica confocal microscope with the excitation wavelength of 340 nm and emission wavelength of 460 nm.

2.9.4.2. Apoptosis Index

Adopting the preceding protocol of cellular uptake in section 2.9.3, HepG2 cells treated with the IC_{50} (24 h treatment) of T-R including its solution, optimized formulations of R-Lipo, R-CO and their blank counterparts were incubated for 24 h at 37℃. Afterward, the cells were fixed and stained by Hoechst 33342 solution according to the previously described procedure in section

2.9.4.1 and were examined under Leica confocal microscope. The results were analyzed with Leica QWin image analysis software (Leica® Microsystems Inc., Germany). Apoptotic cells were featured by nuclear shrinkage, condensation, and fragmentation. Cells from three randomly selected microscopic fields were counted. The apoptosis index (AI) of cells was calculated using the following equation [53]:

$$AI\ (\%)\ =\ (Apoptotic\ cells\ /Total\ cells) * 100 \qquad \textbf{(Equation 6)}$$

2.9.5. Gene expression by quantitative real-time PCR

HepG2 cells were cultured in 12-well plates for 24 h prior to experimentation with different formulations. Cells were then treated for 24 h at 37°C with the IC_{50} (24 h treatment) of T-R including its solution, optimized formulation of R-CO and their blank counterparts. Total RNA was extracted from the cultured cells using TRIzol® Reagent according to the manufacturer's instructions. To estimate RNA concentrations and quality of extracted RNA, A_{260} and A_{280} were measured using NanoDrop 8000 Spectrophotometer (NanoDrop Technologies Inc., Wilmington, USA). Extracted RNA (200 ng) was used as a template for complementary DNA (cDNA) synthesis using COSMO cDNA synthesis reverse transcription (RT)-kit according to the manufacturer's guidelines.

The specific primers pairs used for amplification of NANOG, Bcl-2 target genes and GAPDH were designed using NCBI Primer Blast online software and synthesized via Willowfort® Co., UK. The sequences of forward and reverse primers information are listed in **Table 1**. Quantitative Real-time PCR (qRT-PCR) was performed using 7500 Fast Real-Time PCR System (Thermo Fisher Scientific, Waltham, USA). A final reaction volume of 20 µL was prepared containing 10 µL of HERA^{PLUS} SYBR® Green qPCR Master Mix kit, 5 pmol of each primer and 1 µL of template (cDNA). The default qRT-PCR was performed according to the following thermal cycling conditions: Pre-denaturation at 95 °C for 3 min followed by 40 cycles of amplification including denaturation at 95 °C for 15 s, annealing and primer extension at 60°C for 30 s for both NANOG and GAPDH while for Bcl-2, annealing at 54 ℃ for 15 s and extension at 72 °C for 20 s. Reactions are run a triplicate. Finally, post-PCR melting and amplification, curve analyses were performed for all samples over a gradient extending from an annealing to a denaturation temperature.

The changes in fluorescence of SYBR green dye in every cycle were monitored, and the cycle threshold (C_t) above background for each reaction was calculated. Relative quantities of each target gene were calculated from triplicate samples after normalization of the data against a constantly expressed housekeeping gene GAPDH. Relative gene expression level was calculated for each marker using the $2^{-\Delta\Delta Ct}$ method [54]:

$$2^{-\Delta\Delta Ct} = 2^{-[\Delta Ct\ (treated\ cells) - \Delta Ct\ (control\ cells)]} \quad \textbf{(Equation 7)}$$

where 2 corresponds to the amplification efficiency where the template doubles in each cycle during exponential amplification. NANOG, Bcl-2 and GAPDH mRNA levels were expressed as C_t values. C_t value of each target gene (NANOG and Bcl-2) was normalized to C_t value of the housekeeping gene GAPDH and then the fold change ($\Delta\Delta C_t$) for each gene from each treatment group compared to the control group (untreated cells) was calculated. All measurements were performed in triplicates.

2.10. Statistical analyses

All experiments were performed in triplicates, unless otherwise stated, and the data were expressed as the mean ± standard deviation (SD). Statistical differences were carried out using unpaired Student's t-test and one-way ANOVA followed by Tukey's multiple comparison test as post-hoc analysis using GraphPad Prism (Version 7.04, San Diego, CA, USA). Unless otherwise mentioned, statistical values of $p \leq 0.05$ were considered significant.

3. Results and Discussion

3.1. T-R HPLC assay

The analytical method was validated concerning linearity, specificity, precision, limits of detection and quantification, and recovery. T-R was quantified from the standard calibration curve fitting the equation ($Y = 106.4X + 16.72$), ($R^2 = 0.9997$), covering linearity concentration range of 0.5–25 µg/mL. The lower limit of quantification was 0.5 µg/mL, the intra-day and inter-day precision were less than 2.1 %, while the % recoveries ranged from 96.57 to 102.00 %.

3.2. In-vitro stability of T-R

Owing to the reported low *in-vitro* stability of T-R [20], we screened different aqueous buffers to ensure integrity of T-R without degradation during formulation or dissolution studies.

In this regard, saturated solubilities of T-R at pH 5.5, 6.8 and 7.4 were found to be 28.71 ± 1.34 µg/mL, 27.89 ± 0.74 µg/mL, and 18.06 ± 1.12 µg/mL, respectively, which were consistent with previous reports [6, 55].

For stability studies, and as evident from **Fig. 1**, the higher pH, the higher the degradation of T-R. This result was in good agreement with the previous report [19], the degradation of T-R was demonstrated to be extremely altered in aqueous solutions at different pH levels, being relatively stable in acidic buffer and compromised in alkaline media. At pH 5.5 or pH 6.8, the saturated T-R solution was stable for 2 days. However, at the 3rd day, the concentration of T-R in pH 6.8 relatively declined in comparison with acetate buffer (pH 5.5). In contrast, T-R concentration at pH 7.4 distinctly declined reaching 20% of its initial concentration after 3 days. The degradation rate observed after 72 h in buffer of pH 7.4 was significantly higher ($p \leq 0.01$) as compared with either pH 6.8 or 5.5. Results were in line with published work reporting the influence of pH on the chemical stability of T-R [20]. The degradation mechanism depends on the degree of dissociation of T-R hydroxyl groups where the presence of phenate ions in the structure of T-R render it to be more susceptible to oxidation owing to electrophilic attack, resulting in the formation of the phenoxy radical which eventually leads to the formation of several secondary degradation products [56]. On the other hand, T-R is stable at low pH as its hydroxyl groups are protected from radical oxidation by positively charged H_3O^+ [18].

Notably, saturated solubility of T-R at pH 5.5 or pH 6.8 was about 30 µg/mL, whereas T-R solubility was 40% lower in phosphate buffer (pH 7.4). One reason for this finding might be the inferior T-R stability at pH 7.4, where solution-state degradation interferes with the measurability of *trans*-isomer leading to complex experimental determination of its solubility. From these perspectives, all experimental studies including formulation development, optimization, release profile and shelf-stability or biological activity assays were performed in the most favorable pH 5.5.

3.3. Formulation of T-R-loaded nanocarriers

3.3.1. Anionic liposomes

Lipoid® S75 was selected as a natural candidate of negatively charged phospholipid, imparting a negative zeta potential to liposomal surface at pH of 5.5, providing safety and biocompatibility with T-R. Cholesterol was included to stabilize the bilayer membrane of SUVs

in the dispersion [57]. Liposomes prepared via thin film hydration method were further exposed to probe sonication; the most extensively used technique, for the preparation of SUVs [58]. The probe sonication step following thin film hydration is often associated with low entrapment efficiency, probable degradation of phospholipids and encapsulated sensitive drugs, elimination of large metal contaminants from probe tip, and presence of MLVs along with SUVs [32]. On the other hand, ethanol injection method provides stable nano-sized SUVs with homogenous size distribution through drop-wise addition of dissolved ethanolic lipophilic substances into an aqueous buffer upon magnetic stirring, converting MLVs into SUVs [58].

As demonstrated in **Table 2**, the liposomes prepared by thin film hydration method; R-Lipo 1, possessed hydrodynamic diameter of 188.95±1.48 nm, PDI ~ 0.2 and exhibited negative zeta potential of -54.25±1.39 mV. On the other hand, R-Lipo 4 formulation, produced via ethanol injection technique, was nano-size homogenously distributed unilamellar vesicles (120.18±1.07 nm and PDI <0.15) and possessed relatively higher negative zeta potential of -61.31±2.34 mV. In terms of entrapment efficiency, R-Lipo 4 exhibited relatively higher EE (97.74±0.23%) compared to R-Lipo 1 (93.16±0.82%). Moreover, the yield was significantly influenced by the aforementioned aspects involving multi-steps to produce SUVs along with technical attributes of the preparation methods. R-Lipo 4 provided substantially higher yield (93.61±0.45%) compared to 75.29±1.2% for R-Lipo 1, indicating a preferable industrial scalability of SUVs prepared by ethanol injection rather than thin film hydration method. Accordingly, R-Lipo 4 was selected as the optimal liposomal formulation that could serve as precursor for subsequent nanocochleates formation.

3.3.2. Nanocochleates

Divalent cations including Ca^{2+}, Mg^{2+}, etc., can be used for formation of nanocochleates. However, it has been reported that Ca^{2+} ions possess the ability to produce more firmly packed, highly organized and less hydrated assemblies than Mg^{2+} ions and in much lower concentrations [36]. Moreover, Ca^{2+} is the most biocompatible candidate extensively reported for formulating nanocochleates [37] and it plays an essential role in natural membrane fusion phenomena whereas others are considered unsuccessful in such events [59]. Accordingly, Ca^{2+} was used in this current work to develop T-R-loaded nanocochleates.

The average size of nanocochleates produced from SUVs precursors prepared by thin film hydration method; R-CO 2 and R-CO 3, increased with increasing the final Ca^{2+} concentrations from 9 to 16.67 mM to be 225.76±6.12 nm or 259.45±4.73 nm, respectively. Similarly, the PDI values slightly increased from 0.298±0.024 to 0.367±0.016 as shown in **Table 2**. The PDI values of nanocochleates were relatively higher compared to liposomal counterparts. This can be justified taking in consideration the nanocochleates morphological structure being cigar-like structures that are elongated in length while possessing a very small radius. This renders the hydrodynamic diameters measured more widely dispersed compared to spherical liposome with narrow polydispersity [60]. Adjacent to such increase in size and poly dispersity, gradual reduction in negative zeta potential values indicated the formation of nanocochleates with -43.17±1.28 mV for R-CO 3 with final 16.67 mM Ca^{2+}. As shown in **Table 2**, slight improvements in %EE and % yield were detected in nanocochleates; R-CO 2 and R-CO 3 compared to the starting liposomes; R-CO 1. The loading capacity of T-R was not significantly different between liposomes and nanocochleates due to the minute content of calcium used.

Similarly, a gradual increase of the final Ca^{2+} concentrations (6-26 mM) added to SUVs produced via ethanol injection technique, resulted in an increase in the nanocochleates mean particle size ranged from 126.56±0.89 nm (R-CO 5) to 295.67±5.42 nm (R-CO 8) and this in turn was reflected on PDI values reaching above 0.45 in case of R-CO 8. On the other hand, the negative zeta potential values of nanocochleates decreased as a function of gradient increase in calcium concentrations, ranging from -57.29±2.66 mV to -32.19±0.86 mV. Unlike nanocochleates produced via thin film hydration, changes in the EE % and yield % for formulations produced by ethanol injection were not statistically different, and all formulations produced via ethanol injection possessed more than 98% EE and 95% overall yield.

It is worth noting that the average size of blank nanocochleates counterpart (B-CO 7) was found to be 87.34±2.49 nm. The increase in mean size of nanocochleates after loading with T-R could be a result of the maximum embedment of T-R molecules within the lipid bilayers of nanocochleates' spiral sheets.

Based on these results, R-CO 7 was selected as the optimal nanocochleates formulation possessing a desirable nanometric size of 163.27±2.68 nm, a reasonable PDI of 0.25, a marked negative zeta potential of -46.62±1.12 mV. It also demonstrated a high EE of 99.69±0.12% as well

as a superior product yield of 98.13±1.54%. To the best of our knowledge, this study is the first to report the development of self-assembled nanocochleates; precipitates of Ca^{+2}-bridged soybean PC vesicles loaded with T-R using the trapping method.

3.4. In-vitro evaluation of T-R-loaded nanocarriers

3.4.1. Morphological examination

SEM investigation was performed to examine the surface morphology of R-Lipo 4 and R-CO 7. As evident in **Fig. 2 (I)a**, spherical-shaped vesicles represented conventional liposomes of a mean diameter of 109.41±8.67 nm close to their average size using zeta sizer whereas **Fig. 2 (I)b** revealed elongated cylindrical structures of nanocochleates that exhibited relative adhesion and superimposition of the rods upon vacuum drying inside SEM machine. Using Image J software, the average widths and lengths of these cylindrical structures were estimated to be 42.7±5.16 nm and 420.36±28.91 nm, respectively. Accordingly, SEM images confirm the external distinguishable shape of nanocochleates in which the length to width aspect ratio was markedly changed from spherical liposomes as previously reported [46, 61].

The structure of liposomes and nanocochleates was further scrutinized by examination under TEM and the measured diameters of liposomes were in accordance with the dynamic light scattering (DLS) measurements. On the other hand, the electron photographed of nanocochleates showed a lower mean diameter relative to their zeta sizer measurements owing to alteration in the geometry of nanocochleates' cylinders from the ideal spherical shape used in DLS analysis of particle size. As evident in **Fig. 2 (II)c**, TEM confirmed the presence of long cylinders of R-CO 7 in addition to its unique snail-resembled structures of nanocochleates comprising no internal aqueous space as indicated by the arrows in **Fig. 2 (II)d**. Interestingly, the average length of inter-rolling layer spaces within blank and R-CO 7 nanocochleates was 2.5±0.09 nm and 2.2±0.01 nm, respectively, indicating the minimal interior aqueous spaces.

3.4.2. Solid-state characteristics

3.4.2.1. Differential scanning calorimetry

DSC scanning was performed to study the physicochemical properties of nanocarriers and the potential T-R-excipient interactions. Moreover, it was used to define the physical state of the incorporated T-R in liposomes and nanocochleates, which can impact the mechanism of release.

Thermograms of T-R, T-R-loaded nanocarriers and their corresponding physical mixtures are shown in **Fig. 3 (I)**. It was observed that T-R exhibited a single sharp endothermic peak at 267.5 °C (ΔH= 294.1 J/g) corresponding to melting point of its crystalline structure previously reported [62]. Hence, the sharpness and shape of drug peak reveals the high purity of T-R and suggests a predominantly crystalline behavior. The drug peak was detected in the physical mixtures thermograms (b and d) as demonstrated in **Fig. 3 (I)**, indicating no physicochemical interaction between T-R and other components of liposomes or nanocochleates. On the other hand, the DSC thermograms of R-Lipo 4 and R-CO 7 formulations (c and e), show the disappearance of endothermal peak of T-R suggesting incorporation of T-R in an amorphous or molecularly dispersed state in the nanocarriers. It can be concluded that encapsulation of T-R was in an amorphous state which is expected to enhance solubility, dissolution and release.

3.4.2.2. Fourier-transform infrared spectrometry

FTIR spectroscopy was conducted to elucidate the intermolecular interaction between T-R and excipients used. For comparative purposes, soybean PC and cholesterol were included in the analysis and all spectrum curves of liposomes, nanocochleates and their respective physical mixtures are illustrated in **Fig. 3 (II)**.

The FTIR spectrum of soybean PC (Lipoid® S75) displayed characteristic peaks at 3386 cm^{-1} (broad absorption band of -OH stretching), 2925 and 2855 cm^{-1} (C-H stretching of fatty acid backbone), 1739 cm^{-1} (C=O stretching of the ester group), 1467 cm^{-1} (C-H bending of hydrocarbon chain), 1236 cm^{-1} (C-N stretching band) and 1090 cm^{-1} (C-O stretching) were detected. Cholesterol spectrum revealed an intense and broad absorption peak approximately at 3402 cm^{-1} due to hydroxyl group stretching. Also, it showed a typical band between 2867−2934 cm^{-1} representing stretching vibrations of $-CH_2$ and $-CH_3$ groups. Additionally, bands at 1466 and 1057 cm^{-1} were revealed due to vibrations of C-H bending and C-O stretching, respectively. Similar FTIR spectra of lipid components were previously reported [63]. The spectrum of T-R shows an intense and broad absorption peak of phenolic -OH stretching at 3213 cm^{-1}. The absorption peaks at 1606 cm^{-1} and 1586 cm^{-1} corresponded to C=C stretching of the benzene ring and the band at 1147 cm^{-1} indicated C-O bond stretching. The bending band at 987 cm^{-1} was attributed to the unique olefinic C=C group in the *trans*-configuration of T-R. The bands at 831

cm^{-1} and 675 cm^{-1} referred to the aromatic =C-H bending. Similar FTIR spectrum of T-R was previously reported [63-65].

The FTIR spectra of the physical mixtures of either conventional liposomes or nanocochleates showed combination peaks for the comprising components, confirming the lack of chemical interaction. Likewise, the spectra of R-Lipo 4 and R-CO 7 formulations displayed the major peaks of the components, indicating no significant physicochemical interaction between T-R and other ingredients in physical mixtures or upon processing. Conclusively, these findings generally confirm the standard chemical structure of T-R and its further incorporation in nanocochleates with no compromise to its chemical stability. This is owing to nanocochleates' unique ability of efficient T-R entrapment within their coiled crystal matrix instead of chemically bonding with the drug.

3.4.3. In-vitro release study

In-vitro release of T-R from R-Lipo 4 and R-CO 7 formulations was investigated using dialysis bag diffusion technique. As predicated, the suspension of T-R in acetate buffer (pH 5.5) showed a slower rate of dissolution than that of liposomes and nanocochleates, with approximately 20% and 38% of cumulative T-R released after 6 and 24 h, respectively, which could be attributed to the weak aqueous solubility of T-R in PBS medium.

As demonstrated in **Fig. 4**, R-Lipo 4 exhibited an initial burst release of 13.5% after 15 min, while almost 96% of the initial T-R content was released after 24 h. On contrast, the release of R-CO 7 didn't exhibit an initial burst; about 5% and 7.5% were observed after 15 and 30 min, respectively suggestive of minimal amount of T-R adsorbed on the surface of nanocochleates and is a strong indication of incorporation of T-R within the inner core comprised of spiral layers of the nanocochleates compared to liposomes. The release of T-R from nanocochleates reached approximate values of 28% and 35% after 4 and 6 h compared to 53 and 65%, respectively, from liposomes. This suggested that the release of T-R from nanocochleates was more controlled than that from liposomes. The controlled release phase could be triggered by the slow uncoiling of folded nanocochleates' matrix to facilitate T-R diffusion [66]. Collectively, T-R release from nanocochleates exhibited a biphasic release profile with initial release;14% in 1h, followed by sustained release up to 72 h compared to 25% burst and 100% released in 24 h from liposomes. Therefore, the sustained release behavior of nanocochleates can be useful for many drugs with

poor solubility including T-R as the drug will be slowly introduced GI fluids to be readily absorbed and thereafter leading to enhancement of oral bioavailability [67].

Altogether, these findings signified that the solid rigid structure of nanocochleates succeeded in maintaining T-R within the interior of the multilayered rolls avoiding its rapid leakage. This, in turn, gradually introduced T-R to the media and contributed to the overall stability of available T-R in the release medium.

3.4.3.1. Fitting of kinetic models

To conclude the release mechanism of T-R from R-Lipo 4 and R-CO 7, the release profiles were fitted to three different kinetic models; First order, Higuchi and Korsmeyer–Peppas models as shown in **Table 3**. Regarding the correlation coefficient (R^2), Higuchi model best described the release pattern of T-R suspension, whereas First order and Korsmeyer–Peppas models denoted the best fitting release models for liposomes and nanocochleates formulations, respectively. R^2 values of Higuchi and Korsmeyer–Peppas models were very close to each other in case of T-R suspension and nanocochleates. However, since Korsmeyer–Peppas model has the same functional form and more degrees of freedom than Higuchi model [68], the former model best described the release of T-R from suspension. Additionally, the release exponent values (n) of the Korsmeyer–Peppas model were found to be less than 0.5 for all nanocarrier formulations and equal to 0.5 in case of T-R suspension.

Overall, these results emphasized that the release of T-R from both liposomes and nanocochleates was controlled by Fickian diffusion mechanism which was concordant with the release kinetics from other investigated T-R nanoformulations [16].

3.4.4. Shelf-stability study

As illustrated in **Fig. 5 (I)**, the particle size of the reconstituted lyophilized liposomes powders (R-Lipo 4) significantly increased after 1 and 3 months reaching 616.7% of their initial size compared to a maximum increase of 16.2% for nanocochleates after 6 months. This was concurrent with a significant increase in the value of PDI up to 0.81 in liposomes unlike nanocochleates which maintained a tight polydispersity value about 0.28 after 6 months of storage. These upshots could be ascribed to the pronounced aggregation of the liposomal vesicles upon lyophilization. Moreover, R-Lipo 4 formulation suffered from significant reduction of negative

zeta potential values from -61.3 to approximately -20.1 mV unlike nanocochleates that had a reduction from -46.6 to -36.4 mV after 6 months. Notably, freeze-dried R-Lipo 4 showed a significant decrease in the encapsulation efficiency of T-R, indicating that drug leakage might occur upon reconstitution. Unlike liposomes, no significant change in the entrapment efficiency of lyophilized R-CO 7, being about 99.5% throughout the storage period. This emphasized the outstanding capability of nanocochleates for embedding T-R inside their spiral cylindrical structures upon lyophilization for longer storage periods.

Contrary to conventional liposomes, these outcomes evidenced that R-CO 7 could be physically stable at room temperature following lyophilization without any cryoprotectant for 6 months. As seen in **Fig. 5 (II)**, these results were supported by TEM images which revealed stable nanosized, monodispersed and rolled-up structures of freeze-dried nanocochleates powder after 6 months storage. Nanocochleates maintained their original dimensions unlike liposomes which extensively increased in particle size. In contrast to liposomes, nanocochleates can be lyophilized without disfiguring their unique structure, which offer the feasibility to be stored for long periods of time at room temperature [66]. Moreover, the lipid phase of nanocochleates was firmly arranged in the all *trans* configuration and was extremely mobility-restricted compared with the liquid crystalline phase. Such tight packing should enhance mechanical stability [69]. It is concluded that nanocochleates-based nanoplatform served as a stable free-flowing powder that can be either used in capsules for oral administration or reconstituted for IV injection.

3.5. Permeation studies

3.5.1. Caco-2 permeation

The Caco-2 cell model, which acts like small intestine epithelium, is considered a pivotal tool for investigating the rate of drug permeation [70]. Thus, the application of the Caco-2 model for the *in-vitro* assessment of drug-encapsulated nanocarriers is a useful resource to infer the oral bioavailability. Confocal laser scanning microscope (CLSM) images of Caco-2 cells obtained 9 days after initiation of the cultures revealed that the cells were well spread over the Transwell® inserts, nevertheless the cell density was too low to attain confluent monolayers as illustrated in **Fig. 6 (I)a**. However, after 21 days; at the end of the transport studies, the cells formed a dense monolayer lacking intercellular spaces as shown in **Fig. 6 (I)b**. Furthermore, it was worth noting that the cells emerged to be compressed since each cell nucleus occupied a smaller surface area

than in **Fig. 6 (I)a**. These observations confirmed the maintenance of Caco-2 monolayer integrity throughout the transport intervals of the experiment. Furthermore, the TEER values were measured at the beginning and end of the transport studies with no significant variation in the TEER readings as shown in **Table 4**, implying that the integrity of Caco-2 monolayers during the transport studies.

Plain T-R suspension, R-Lipo 4 and R-CO 7 were individually dispersed in the apical compartment and the cumulative amounts of T-R permeated through Caco-2 monolayers were calculated at different time intervals over 24 h to delineate the transport profiles as illustrated in **Fig. 6 (II)**. As seen, R-CO 7 displayed significantly higher permeation rate; 81% of T-R was transported across the Caco-2 monolayer after 24 h. Conversely, T-R suspension and R-Lipo 4 showed lower T-R transport rates; 17% and 42%, respectively.

The apparent permeability coefficient (P_{app}) for all the tested samples was calculated using the linear portion of the transport curves as demonstrated in **Table 4**. The transport efficiency of nanocochleates was significantly higher; 1.8 and 4.1-folds relative to conventional liposomes and T-R suspension, respectively. This finding could be attributed to the pronounced competence of nanocochleates to open intercellular tight junctions and paracellular pathway which was supported by down-regulation of cellular tight junction proteins including ZO-1, F-actin and claudin-4 as previously reported [71]. Moreover, another postulation put forward was demonstrated that nanocochleates were taken up by Caco-2 cells via clathrin- and caveolin-mediated endocytosis [71]. It is worth noting that there was no difference in TEER values of Caco-2 monolayers in this study, suggestive of intact layers and implying confidence in the integrity of the monolayers as permeation membranes. Taken altogether, these findings evidenced the prominent potential of nanocochleates to enhance the permeability of T-R when administered orally compared to conventional liposomes.

3.5.2. Ex-vivo permeation using the rat intestine

Ex-vivo permeation techniques are widely used for assessment of human intestinal absorption. Among these methods, the non-everted intestinal sac model possesses several merits. These include simplicity, feasibility of using relatively small amounts of drug, minimum morphological damage to the intestine and most importantly, frequent sampling with ease of quantitative analysis [50]. As shown in **Fig. 6 (III)**, T-R from suspension showed a low permeation

across the intestinal epithelium; 131.56±18.91 µg in 2 h. In fact, the direct addition of pure T-R to the buffer solution immediately formed crystals and precipitates leading to inferior permeability. On the other hand, R-Lipo 4 showed a significantly higher permeation rate of T-R than drug suspension with 285.23±16.94 µg permeated after 2 h. A suggested mechanism by which liposomes could confer better penetration of T-R throughout the intestine, is the interaction between the phospholipid head's functional groups and epithelial mucous resulting in an alteration in its viscosity after rearrangement of mucin molecules [72, 73].

For nanocochleates, higher amounts of T-R permeated after 30 min; 177.25±7.49 µg as compared to 26.15±8.64 µg and 82.5±7.98 µg from suspension and liposomes, respectively. Furthermore, T- R permeation from nanocochleates continued to increase to 473.75±11.89 µg after 2 h which was significantly higher than permeation from suspension or liposomes as shown in **Fig. 6 (III)**, achieving superior P_{app} value as demonstrated in **Table 4**. Interestingly, nanocochleates significantly enhanced *ex-vivo* permeation of T-R with 2.1 and 6.5-folds higher compared to conventional liposomes and native T-R suspension after 60 min, respectively. The intensified permeability of nanocochleates could be ascribed to the membrane fusion capability which can be proposed as membrane fusion intermediates in several naturally occurring membrane fusion events [74]. Additionally, the high tension of nanocochleates edges, compared to edge-free spherical liposomes, is possibly the driving force which evokes them to interfere with the cell membrane [75]. Furthermore, this was consistent with the estimated mechanism by which nanocochleates could enhance the oral permeability through opening tight junctions of Caco-2 cells and allowing for paracellular transport [71]. In conclusion, these data corroborated that nanocochleates possess an efficient potential of enhancing oral permeability of T-R through the intestinal epithelium compared to conventional liposomes.

3.6. Anticancer activity

In order to translate the application of an orally administered T-R-loaded nanocochleates to the tumor site in a living host, *in-vitro* assays of anticancer activity were investigated on human liver cancer cell line. Several reasons could justify the applicability of such evaluations despite the ambiguity of the potential fate nanocochleates might be introduced to, in an *in vivo* situation. These include the capability of nanocochleates of opening intercellular tight junctions and paracellular pathway and their uptake by Caco-2 cells via clathrin- and caveolin-mediated endocytosis as

discussed in section 3.5. The internal layers of nanocochleates remained intact while being transported inside endocytic vesicles; only the outer layers might be disturbed (section 3.5.2). Owing to the high tension of nanocochleates edges compared to the edge-free spherical liposomes, the external layers of nanocochleates would fuse with the membrane of epithelial cells keeping T-R embedded within the interior layers. This supports that the remaining T-R-loaded rolls could enter the systemic circulation reaching blood supply of the tumor site. Most importantly, the structure of nanocochleates remains intact in absence of Ca^{+2} concentration fluctuations while permeating across the intestinal epithelium. Once inside the target tumor cell, the low calcium concentration could trigger the slow uncoiling of the rolled layers of nanocochleates releasing the encochleated T-R. On top of that, nanocochleates are known to facilitate lymphatic absorption of drugs [76]. The lipid roll gets assembled in the core of chylomicron by enterocytes and enters the lymphatic system thereby reaching lymph nodes which frequently harbor metastases. Afterwards, they travel to the thoracic duct and enter the blood stream which further delivers the encochleated T-R to the tumor environment in liver. Furthermore, nanocochleates could be readily available at the tumor site via their extravasation through the tumor porous capillary endothelium caused by enhanced permeability and retention [44, 76].

3.6.1. Cell proliferation assay

Cytotoxicity studies of T-R, R-Lipo 4, R-CO 7 and their blank counterparts were investigated on human liver cancer HepG2 cells over periods of 24 and 48 h using MTT assay. The experiments were performed at different concentrations of T-R solution or amounts of liposomes or nanocochleates containing equivalent concentrations of the drug, as illustrated in **Fig. 7 (I)**. The values of IC_{50}; defined as a quantitative assessment of a drug concentration necessary for inhibition of a biological response by half, were calculated by using GraphPad Prism (version 7.04).

As for the equivalent volume (range: 0.7-55 µL/mL) of applied T-R-loaded nanocarriers, blank formulations of either liposomes or nanocochleates exhibited no significant cytotoxicity against HepG2 cells similar to the control up to 38.5 µL/mL which was indicative of good biocompatibility. However, there was a slight toxicity of blank counterparts of either liposomes or nanocochleates to cancer cells (85% of cell viability) at highest examined volume of blank formulations (55 µL/mL). This finding could be referred to the inherent anticancer activity of

phospholipid which was reported to be associated to its unique apoptosis-inducing properties through the generation of reactive oxygen species (ROS) or its direct disturbing influence on the order of cell membrane causing fluidity and leakage [77]. On the other hand, free T-R solution, R-Lipo 4 and R-CO 7 showed a dose- and time-dependent growth inhibition where R-CO 7 possessed a significantly higher antiproliferative activity against HepG2 cells. After 24 h of incubation, the IC_{50} values of T-R, R-Lipo 4 and R-CO 7 were found to be 134.6±3.49, 95.94±2.67 and 66.18±1.89 μM while the IC_{50} values after 48 h were decreased to 54.53±1.76, 40.89±1.01 and 28.35±0.72 μM, respectively. Our findings of IC_{50} values of T-R after treatment for 24 h (134.6±3.49 μM) and 48 h (54.53±1.76 μM) were consistent with previous studies [78, 79]. Notably, the IC_{50} value of R-CO 7 formulation after 24 h treatment was about 1.5 and 2-folds lower than that of R-Lipo 4 formulation and free T-R on HepG2 cells, respectively.

Herein, the cytotoxic superiority of R-CO 7 might be ascribed to higher accumulation of T-R via direct interaction or phagocytosis, fusion between nanocochleates and the cancer cell membrane followed by controlled release of the drug [80].

Regarding this postulation*, in-vivo* concentration of calcium inside cancer cells remained constant as the integrity of nanocochleates structures were preserved [59]. Meanwhile, most of T-R molecules existed within the internal layers of a solid, stable, impermeable structure of nanocochleates. Therefore, once in the interior of a target HepG2 cell, even though, the low calcium concentration triggered the opening of the rolled layers of nanocochleates releasing the encochleated T-R.

According to these results, the improved anticancer activity was exemplified by lower IC_{50} value of R-CO 7 formulation compared to that of free T-R and R-Lipo 4 formulation. This could be attributed to enhanced cellular uptake of nanocochleates and improved solubility of T-R in nanocochleates formulation. Taken all together, nanocochleates demonstrated a substantial enhancement of the anticancer efficacy of T-R against HepG2 cells along with an overall dose reduction and expected improved safety.

3.6.2. Cellular uptake

Following the antiproliferative results in HepG2 cells, the cellular uptake and co-location of T-R-loaded nanocarriers were investigated relying on the inherent green fluorescence properties

of T-R [81]. As revealed in **Fig. 7 (II)**, the uptake of R-Lipo 4 and R-CO 7 formulations through HepG2 cells were shown as green fluorescence, co-existing with the blue Hoechst-stained cell nuclei. It was found that liposomes and nanocochleates demonstrated an equivalent uptake of T-R in HepG2 cells after incubation for 1 h with the corresponding IC_{50} at 24 h of each formulation. However, the cellular uptake of nanocochleates was based on lower concentration of T-R (66.18±1.89 μM ≡ IC_{50} of 24 h-treatment) as compared to conventional liposomes (95.94±2.67 μM ≡ IC_{50} of 24 h-treatment). The nuclei of HepG2 cells in the treatment groups of liposomes and nanocochleates appeared equally normal, spherical with intact outline similar to the control group.

This emphasized the relative safety of T-R-loaded nanocochleates whilst augmenting the anticancer activity at lower dose compared to free T-R solution or conventional liposomes. Furthermore, CLSM observations supported that HepG2 cells demonstrated a significantly higher internalization of R-CO 7 formulation compared to free T-R and R-Lipo 4 formulation at an equivalent IC_{50} (24 h-treatment) of free T-R (134.6±3.49 μM) after 1 h of incubation which were also confirmed by 3D surface plots analyzed via Image J 1.52a software, as shown in **Fig. 8 (I)**. Moreover, the confocal images depicted 5 and 74-folds increase of T-R uptake from nanocochleates than that of conventional liposomes and free T-R, respectively, as evident in **Fig. 8 (II)**. Thus, nanocochleates showed a significant ($p \leq 0.0001$) higher fluorescence intensity than that of conventional liposomes and free T-R which demonstrated a moderate and weak fluorescence signals in HepG2 cells after 1 h of incubation, respectively.

The potential mechanism of cellular internalization could be ascribed to the fusion between the outer layer of nanocochleates and cancer cell membrane [74]. A close contact of the calcium-rich, highly organized membrane of a nanocochleate with a natural membrane might have caused membrane reordering. This consequently might have introduced a small amount of T-R into the cytoplasm of the target HepG2 cell. After that, nanocochleate liberated off the cell could be ready for another fusion event, either with this or another hepatoma cell. Thereby, nanocochleates may be taken up by endocytosis and escape from the endocytic vesicle to deliver the encochleated T-R into the cytosol of target tumor cell in a controlled pattern [74]. Overall, these observations supported that T-R could be profusely taken up by the treated HepG2 cells which was accounted for the superior cellular internalization and cytosolic delivery of nanocochleates when compared to conventional liposomes or free T-R.

3.6.3. Cell apoptosis

Apoptosis, programed cell death, is a well-known phenomenon that has been recognized as a major antitumor therapeutic response [82]. The therapeutic efficacy of T-R against HCC has often been attributed to antiproliferative and pro-apoptotic effects [83]. Since R-CO 7 formulation exerted an efficient anticancer activity against HepG2 cells, we further explored whether delivering T-R via nanocochleates would augment cellular apoptosis.

As illustrated in **Fig. 9 (I)**, CLSM images of HepG2 nuclei revealed that 24 h incubation with R-CO 7 treatment group at 24 h IC_{50} of free T-R computed at section 3.6.1 induced progressive cellular apoptosis than that of either free T-R or R-Lipo 4. This was observed as the characteristic hallmarks of cell apoptosis including nuclear margination, chromatin condensation, nuclear fragmentation, membrane blebbing, membrane loose and finally the breakdown of the cell into smaller units called apoptotic bodies [54] were evidently visible. Moreover, the percent of AI in the 24 h R-CO 7-treated HepG2 cells, was significantly ($p \leq 0.0001$) higher; 1.7 and 3.8-folds than that of R-Lipo 4 and free T-R, respectively, as illustrated in **Fig. 9 (II)**.

Remarkably, blank formulations; B-Lipo and B-CO 7, displayed normal HepG2 nuclei along with AI percent equivalent to the control group as evident in **Fig. 9 (I) and (II)**, indicating that cell apoptosis was only induced via enhancing the anticancer activity of T-R. Accordingly, these findings supported that nanocochleates significantly induced higher cellular apoptosis compared to free T-R or conventional liposomes, which ultimately resulted in augmenting the anticancer efficacy of T-R for management of HCC.

3.6.4. Gene expression using qRT-PCR

The Bcl-2 class members including Bax and Bcl-2, act as critical modulators of the mitochondrial-dependent apoptotic pathway where Bcl-2 is responsible for negative regulation of cell apoptosis and promotion of cell survival [84]. T-R-induced apoptosis has been ascribed to interference with the Bcl-2/Bax, apoptotic pathway [78]. On the other hand, NANOG gene is a key transcription factor regulating both embryonic and cancer stem cells and also is recognized as a prognostic marker in HCC [85]. Moreover, upregulation of NANOG expression in HCC is often associated with resistance to chemotherapeutic agents such as sorafenib and cisplatin along with a

notable capacity for tumor invasion, metastasis and high mortality rate [85]. Therefore, NANOG expression has emerged as a potential therapeutic target for many anticancer agents.

Recently, T-R was proved to suppress the expression of cancer stem cell markers including NANOG in glioblastoma, head and neck cancer, and pancreatic cancer [86-88]. However, and to the best of our knowledge, the influence of T-R on NANOG expression has not been yet published in HCC.

As demonstrated in **Fig. 10 (I)**, qRT-PCR results revealed that 24 h treatment with R-CO 7 formulation resulted in significant downregulation of Bcl-2 ($p \leq 0.0001$) 13-fold lower than that of free T-R in HepG2 cells. Most importantly, the downregulation of Bcl-2 expression was concordant with CLSM observation of cell apoptosis in HepG2 cells. Similarly, R-CO 7-treated HepG2 cells exhibited a significant downregulation in NANOG expression level after 24 h ($p \leq 0.001$); 2-fold lower than that of free T-R, as evident in **Fig. 10 (II)**. Such downregulation of NANOG expression is probably involved in the antiproliferative effect of T-R. Concerning Bcl-2 and NANOG expression levels, there were no significant difference between the treatment group of blank nanocochleates and the control group as shown in **Fig. 10 (I) and (II)**, indicating that placebo nanocochleates possessed no influence on the target genes and that the downregulation of these genes was ascribed exclusively to the improvement of the anticancer efficacy of T-R via nanocochleates.

Taken altogether, these data indicated that nanocochleates have an invaluable potential to augment the anticancer efficacy of T-R by efficient knockdown of anti-apoptotic (Bcl-2) and cancer stemness (NANOG) biomarker genes in HepG2 cells. To the best of our knowledge, the present study is the first to demonstrate the efficient potential of T-R-loaded nanocochleates to suppress NANOG expression in HepG2 cells and also proposes the lipid nanocochleates as a novel therapeutic platform for delivering T-R in the treatment of HCC.

4. Conclusions

In this present study, we report on the successful development of novel T-R-loaded nanocochleates via conversion of PC-based anionic SUVs into self-assembled spiral structures using a well-established simple and reproducible trapping method. The elaborated nanocochleates displayed excellent nanosized and monodispersed rolls that possessed good *in-vitro*

physicochemical characteristics along with high product yield and EE% of T-R available in amorphous highly soluble state. Most importantly, nanocochleates exhibited a long shelf-life stability after lyophilization compared to conventional liposomes. Interestingly, these nanocochleates controlled and sustained the release of T-R that collectively, with the lipophilicity of the nanocarriers, contributed to the enhanced oral permeability using independent Caco-2 transport and *ex-vivo* intestinal permeation models. Appraising optimal preparation and storage condition along with confirmation on the enhanced oral permeability, the anticancer activity against HepG2 was profoundly scrutinized. Increased cellular uptake, compared to conventional liposomes, significantly boosted the antiproliferative efficacy via augmented apoptotic effect. This was supported with significant knockdown of anti-apoptotic; Bcl-2 and cancer stemness; NANOG biomarker genes in HepG2 cells. Altogether, these auspicious outcomes strongly support nanocochleates' inimitable potential to be a promising nanoplatform for efficient oral delivery of T-R as a clinical therapy of HCC with lower dosing frequency, minimal side effects and higher patient compliance. We further envisage that future comprehensive investigations including the molecular mechanisms of enhancing anticancer activity of T-R in liver tumor-bearing animal model, are needed to interrogate the invaluable features of the designed nanocochleates for clinical translation into humans.

Acknowledgments

The authors gratefully acknowledge Lipoid AG (Ludwigshafen, Germany) for generous providing (Lipoid® S75) phospholipid. The authors also would like to thank Dr. Radwa A. Mehanna for scientific and technical support.

CRediT authorship contribution statement

Mohamed G. EL-Melegy: Conceptualization, Methodology, Validation, Formal analysis, Investigation, Resources, Writing - original draft, Writing - review & editing.

Hoda M. Eltaher: Conceptualization, Methodology, Resources, Writing – review & editing, Supervision.

Ahmed Gaballah: Methodology, Investigation of PCR analysis.

Amal H. El-Kamel: Conceptualization, Methodology, Resources, Writing – review & editing, Supervision, Project administration.

All authors approved the final version of the manuscript.

Declaration of financial and competing interest

The authors report no relevant affiliations or financial involvement with any organization or entity with a financial interest or conflict with the main objectives or materials declared in the work.

Data availability statement

The authors confirm that the data for this study findings are available within the article.

References:

[1] J.D. Yang, P. Hainaut, G.J. Gores, A. Amadou, A. Plymoth, L.R. Roberts, A global view of hepatocellular carcinoma: trends, risk, prevention and management, Nature Reviews Gastroenterology & Hepatology, 16 (2019) 589-604. https://doi.org/10.1038/s41575-019-0186-y.
[2] E. Kim, P. Viatour, Hepatocellular carcinoma: old friends and new tricks, Experimental & Molecular Medicine, 52 (2020) 1898-1907. https://doi.org/10.1038/s12276-020-00527-1.
[3] J.M. Llovet, A. Villanueva, A. Lachenmayer, R.S. Finn, Advances in targeted therapies for hepatocellular carcinoma in the genomic era, Nature Reviews Clinical Oncology, 12 (2015) 408-424. https://doi.org/10.1038/nrclinonc.2015.103.
[4] J. Bruix, M. Reig, M. Sherman, Evidence-Based Diagnosis, Staging, and Treatment of Patients With Hepatocellular Carcinoma, Gastroenterology, 150 (2016) 835-853. https://doi.org/10.1053/j.gastro.2015.12.041.
[5] A.M. Mileo, S. Miccadei, Polyphenols as Modulator of Oxidative Stress in Cancer Disease: New Therapeutic Strategies, Oxidative Medicine and Cellular Longevity, 2016 (2016) 6475624. https://doi.org/10.1155/2016/6475624.
[6] A. Amri, J.C. Chaumeil, S. Sfar, C. Charrueau, Administration of resveratrol: What formulation solutions to bioavailability limitations?, Journal of Controlled Release, 158 (2012) 182-193. https://doi.org/10.1016/j.jconrel.2011.09.083.

[7] G. Singh, Resveratrol: nanocarrier-based delivery systems to enhance its therapeutic potential, Nanomedicine, 15 (2020) 2801-2817. https://doi.org/10.2217/nnm-2020-0289.
[8] C. Colica, M. Milanović, N. Milić, V. Aiello, A. De Lorenzo, L. Abenavoli, A Systematic Review on Natural Antioxidant Properties of Resveratrol, Natural Product Communications, 13 (2018) 1195–1203 https://doi.org/10.1177/1934578X1801300923.
[9] Y. Lu, X. Lu, L. Wang, W. Yang, Resveratrol attenuates high fat diet-induced mouse cardiomyopathy through upregulation of estrogen related receptor-α, European Journal of Pharmacology, 843 (2019) 88-95. https://doi.org/10.1016/j.ejphar.2018.10.018.
[10] B. Cote, L.J. Carlson, D.A. Rao, A.W.G. Alani, Combinatorial resveratrol and quercetin polymeric micelles mitigate doxorubicin induced cardiotoxicity in vitro and in vivo, Journal of Controlled Release, 213 (2015) 128-133. https://doi.org/10.1016/j.jconrel.2015.06.040.
[11] E. Öztürk, A.K.K. Arslan, M.B. Yerer, A. Bishayee, Resveratrol and diabetes: A critical review of clinical studies, Biomedicine & Pharmacotherapy, 95 (2017) 230-234. https://doi.org/10.1016/j.biopha.2017.08.070.
[12] M.H. Rahman, R. Akter, T. Bhattacharya, M.M. Abdel-Daim, S. Alkahtani, M.W. Arafah, N.S. Al-Johani, N.M. Alhoshani, N. Alkeraishan, A. Alhenaky, O.H. Abd-Elkader, H.R. El-Seedi, D. Kaushik, V. Mittal, Resveratrol and Neuroprotection: Impact and Its Therapeutic Potential in Alzheimer's Disease, Front Pharmacol, 11 (2020) 619024-619024. https://doi.org/10.3389/fphar.2020.619024.
[13] J.-H. Ko, G. Sethi, J.-Y. Um, M.K. Shanmugam, F. Arfuso, A.P. Kumar, A. Bishayee, K.S. Ahn, The Role of Resveratrol in Cancer Therapy, International Journal of Molecular Sciences, 18 (2017). https://doi.org/10.3390/ijms18122589.
[14] A.Y. Berman, R.A. Motechin, M.Y. Wiesenfeld, M.K. Holz, The therapeutic potential of resveratrol: a review of clinical trials, npj Precision Oncology, 1 (2017) 35. https://doi.org/10.1038/s41698-017-0038-6.
[15] A. Bishayee, T. Politis, A.S. Darvesh, Resveratrol in the chemoprevention and treatment of hepatocellular carcinoma, Cancer Treatment Reviews, 36 (2010) 43-53. https://doi.org/10.1016/j.ctrv.2009.10.002.
[16] N. Summerlin, E. Soo, S. Thakur, Z. Qu, S. Jambhrunkar, A. Popat, Resveratrol nanoformulations: Challenges and opportunities, International Journal of Pharmaceutics, 479 (2015) 282-290. https://doi.org/10.1016/j.ijpharm.2015.01.003.
[17] D. Delmas, V. Aires, E. Limagne, P. Dutartre, F. Mazué, F. Ghiringhelli, N. Latruffe, Transport, stability, and biological activity of resveratrol, Annals of the

New York Academy of Sciences, 1215 (2011) 48-59. https://doi.org/10.1111/j.1749-6632.2010.05871.x.
[18] A. Francioso, P. Mastromarino, A. Masci, M. d'Erme, L. Mosca, Chemistry, Stability and Bioavailability of Resveratrol, Medicinal Chemistry, 10 (2014) 237-245.
[19] Š. Zupančič, Z. Lavrič, J. Kristl, Stability and solubility of trans-resveratrol are strongly influenced by pH and temperature, European Journal of Pharmaceutics and Biopharmaceutics, 93 (2015) 196-204. https://doi.org/10.1016/j.ejpb.2015.04.002.
[20] K. Robinson, C. Mock, D. Liang, Pre-formulation studies of resveratrol, Drug Development and Industrial Pharmacy, 41 (2015) 1464-1469. https://doi.org/10.3109/03639045.2014.958753.
[21] A. Jhaveri, P. Deshpande, B. Pattni, V. Torchilin, Transferrin-targeted, resveratrol-loaded liposomes for the treatment of glioblastoma, Journal of Controlled Release, 277 (2018) 89-101. https://doi.org/10.1016/j.jconrel.2018.03.006.
[22] T. Pentek, E. Newenhouse, B. O'Brien, A.S. Chauhan, Development of a Topical Resveratrol Formulation for Commercial Applications Using Dendrimer Nanotechnology, Molecules, 22 (2017). https://doi.org/10.3390/molecules22010137.
[23] C.-C. Yen, C.-W. Chang, M.-C. Hsu, Y.-T. Wu, Self-Nanoemulsifying Drug Delivery System for Resveratrol: Enhanced Oral Bioavailability and Reduced Physical Fatigue in Rats, International Journal of Molecular Sciences, 18 (2017). https://doi.org/10.3390/ijms18091853.
[24] L. Zhang, K. Zhu, H. Zeng, J. Zhang, Y. Pu, Z. Wang, T. Zhang, B. Wang, Resveratrol solid lipid nanoparticles to trigger credible inhibition of doxorubicin cardiotoxicity, Int J Nanomedicine, 14 (2019) 6061-6071. https://doi.org/10.2147/IJN.S211130.
[25] D.-H. Kuk, E.-S. Ha, D.-H. Ha, W.-Y. Sim, S.-K. Lee, J.-S. Jeong, J.-S. Kim, I.-h. Baek, H. Park, D.H. Choi, J.-W. Yoo, S.H. Jeong, S.-J. Hwang, M.-S. Kim, Development of a Resveratrol Nanosuspension Using the Antisolvent Precipitation Method without Solvent Removal, Based on a Quality by Design (QbD) Approach, Pharmaceutics, 11 (2019). https://doi.org/10.3390/pharmaceutics11120688.
[26] M.T.P. de Oliveira, D. de Sá Coutinho, É. Tenório de Souza, S. Stanisçuaski Guterres, A.R. Pohlmann, P.M.R. Silva, M.A. Martins, A. Bernardi, Orally delivered resveratrol-loaded lipid-core nanocapsules ameliorate LPS-induced acute lung injury via the ERK and PI3K/Akt pathways, Int J Nanomedicine, 14 (2019) 5215-5228. https://doi.org/10.2147/IJN.S200666.
[27] M. Sessa, M.L. Balestrieri, G. Ferrari, L. Servillo, D. Castaldo, N. D'Onofrio, F. Donsì, R. Tsao, Bioavailability of encapsulated resveratrol into nanoemulsion-

based delivery systems, Food Chemistry, 147 (2014) 42-50. https://doi.org/10.1016/j.foodchem.2013.09.088.
[28] J. Shen, N. Zhuo, S. Xu, Z. Song, Z. Hu, J. Hao, X. Guo, Resveratrol delivery by ultrasound-mediated nanobubbles targeting nucleus pulposus cells, Nanomedicine, 13 (2018) 1433-1446. https://doi.org/10.2217/nnm-2018-0019.
[29] M. Rostami, M. Ghorbani, M. Aman mohammadi, M. Delavar, M. Tabibiazar, S. Ramezani, Development of resveratrol loaded chitosan-gellan nanofiber as a novel gastrointestinal delivery system, International Journal of Biological Macromolecules, 135 (2019) 698-705. https://doi.org/10.1016/j.ijbiomac.2019.05.187.
[30] D. Pando, M. Matos, G. Gutiérrez, C. Pazos, Formulation of resveratrol entrapped niosomes for topical use, Colloids and Surfaces B: Biointerfaces, 128 (2015) 398-404. https://doi.org/10.1016/j.colsurfb.2015.02.037.
[31] H.F. Salem, R.M. Kharshoum, H.A. Abou-Taleb, D.M. Naguib, Nanosized Transferosome-Based Intranasal In Situ Gel for Brain Targeting of Resveratrol: Formulation, Optimization, In Vitro Evaluation, and In Vivo Pharmacokinetic Study, AAPS PharmSciTech, 20 (2019) 181. https://doi.org/10.1208/s12249-019-1353-8.
[32] A. Akbarzadeh, R. Rezaei-Sadabady, S. Davaran, S.W. Joo, N. Zarghami, Y. Hanifehpour, M. Samiei, M. Kouhi, K. Nejati-Koshki, Liposome: classification, preparation, and applications, Nanoscale Research Letters, 8 (2013) 102. https://doi.org/10.1186/1556-276X-8-102.
[33] L. Zarif, Elongated supramolecular assemblies in drug delivery, Journal of Controlled Release, 81 (2002) 7-23. https://doi.org/10.1016/S0168-3659(02)00010-X.
[34] S.J. Thornton, K.M. Wasan, The reformulation of Amphotericin B for oral administration to treat systemic fungal infections and visceral leishmaniasis, Expert Opinion on Drug Delivery, 6 (2009) 271-284. https://doi.org/10.1517/17425240902802861.
[35] M. Liu, M. Chen, Z. Yang, Design of amphotericin B oral formulation for antifungal therapy, Drug Delivery, 24 (2017) 1-9. https://doi.org/10.1080/10717544.2016.1225852.
[36] M. Tilawat, S. Bonde, Nanocochleates: A potential drug delivery system, Journal of Molecular Liquids, 334 (2021) 116115. https://doi.org/10.1016/j.molliq.2021.116115.
[37] P. Shende, R. Khair, R.S. Gaud, Nanostructured cochleates: a multi-layered platform for cellular transportation of therapeutics, Drug Development and Industrial Pharmacy, 45 (2019) 869-881. https://doi.org/10.1080/03639045.2019.1583757.

[38] A. Lipa-Castro, V. Nicolas, A. Angelova, G. Mekhloufi, B. Prost, M. Chéron, V. Faivre, G. Barratt, Cochleate formulations of Amphotericin b designed for oral administration using a naturally occurring phospholipid, International Journal of Pharmaceutics, 603 (2021) 120688. https://doi.org/10.1016/j.ijpharm.2021.120688.
[39] M. Asprea, F. Tatini, V. Piazzini, F. Rossi, M.C. Bergonzi, A.R. Bilia, Stable, Monodisperse, and Highly Cell-Permeating Nanocochleates from Natural Soy Lecithin Liposomes, Pharmaceutics, 11 (2019). https://doi.org/10.3390/pharmaceutics11010034.
[40] R.J. Ahiwale, B. Chellampillai, A.P. Pawar, Investigation of 1,2-Dimyristoyl-sn-Glycero-3-Phosphoglycerol-Sodium (DMPG-Na) Lipid with Various Metal Cations in Nanocochleate Preformulation: Application for Andrographolide Oral Delivery in Cancer Therapy, AAPS PharmSciTech, 21 (2020) 279. https://doi.org/10.1208/s12249-020-01801-1.
[41] S. Jagwani, S. Jalalpure, D. Dhamecha, G.S. Hua, K. Jadhav, A Stability Indicating Reversed Phase HPLC Method for Estimation of trans-Resveratrol in Oral Capsules and Nanoliposomes, Analytical Chemistry Letters, 9 (2019) 711-726. https://doi.org/10.1080/22297928.2019.1696227.
[42] C. Righeschi, M. Coronnello, A. Mastrantoni, B. Isacchi, M.C. Bergonzi, E. Mini, A.R. Bilia, Strategy to provide a useful solution to effective delivery of dihydroartemisinin: Development, characterization and in vitro studies of liposomal formulations, Colloids and Surfaces B: Biointerfaces, 116 (2014) 121-127. https://doi.org/10.1016/j.colsurfb.2013.12.019.
[43] S.J. Nadaf, S.G. Killedar, Curcumin nanocochleates: Use of design of experiments, solid state characterization, in vitro apoptosis and cytotoxicity against breast cancer MCF-7 cells, Journal of Drug Delivery Science and Technology, 47 (2018) 337-350. https://doi.org/10.1016/j.jddst.2018.06.026.
[44] C. Bothiraja, B.D. Yojana, A.P. Pawar, K.S. Shaikh, U.H. Thorat, Fisetin-loaded nanocochleates: formulation, characterisation, in vitro anticancer testing, bioavailability and biodistribution study, Expert Opinion on Drug Delivery, 11 (2014) 17-29. https://doi.org/10.1517/17425247.2013.860131.
[45] N. Li, C. Zhuang, M. Wang, X. Sun, S. Nie, W. Pan, Liposome coated with low molecular weight chitosan and its potential use in ocular drug delivery, International Journal of Pharmaceutics, 379 (2009) 131-138. https://doi.org/10.1016/j.ijpharm.2009.06.020.
[46] Shuddhodana, P.W.K. Wong, Z. Judeh, Continuous, high-throughput production of artemisinin-loaded supramolecular cochleates using simple off-the-shelf flow focusing device, Materials Science and Engineering: C, 108 (2020) 110410. https://doi.org/10.1016/j.msec.2019.110410.

[47] Y. Zhang, M. Huo, J. Zhou, A. Zou, W. Li, C. Yao, S. Xie, DDSolver: An Add-In Program for Modeling and Comparison of Drug Dissolution Profiles, The AAPS Journal, 12 (2010) 263-271. https://doi.org/10.1208/s12248-010-9185-1.
[48] W.L. Hayton, T. Chen, Correction of perfusate concentration for sample removal, Journal of Pharmaceutical Sciences, 71 (1982) 820-821. https://doi.org/10.1002/jps.2600710726.
[49] P. Palumbo, U. Picchini, B. Beck, J. van Gelder, N. Delbar, A. DeGaetano, A general approach to the apparent permeability index, Journal of Pharmacokinetics and Pharmacodynamics, 35 (2008) 235. https://doi.org/10.1007/s10928-008-9086-4.
[50] Z. Luo, Y. Liu, B. Zhao, M. Tang, H. Dong, L. Zhang, B. Lv, L. Wei, Ex vivo and in situ approaches used to study intestinal absorption, Journal of Pharmacological and Toxicological Methods, 68 (2013) 208-216. https://doi.org/10.1016/j.vascn.2013.06.001.
[51] C.S. Kumar, M.D. Raja, D.S. Sundar, M. Gover Antoniraj, K. Ruckmani, Hyaluronic acid co-functionalized gold nanoparticle complex for the targeted delivery of metformin in the treatment of liver cancer (HepG2 cells), Carbohydrate Polymers, 128 (2015) 63-74. https://doi.org/10.1016/j.carbpol.2015.04.010.
[52] B. Chazotte, Labeling Nuclear DNA with Hoechst 33342, Cold Spring Harbor Protocols, 2011 (2011) pdb.prot5557. https://doi.org/10.1101/pdb.prot5557
[53] Z. Qu, Y. Zhang, M. Liao, Y. Chen, J. Zhao, Y. Pan, In vitro and in vivo antitumoral action of metformin on hepatocellular carcinoma, Hepatology research : the official journal of the Japan Society of Hepatology, 42 (2012) 922-933. https://doi.org/10.1111/j.1872-034X.2012.01007.x.
[54] S. Khazaei, N.M. Esa, V. Ramachandran, R.A. Hamid, A.K. Pandurangan, A. Etemad, P. Ismail, In vitro Antiproliferative and Apoptosis Inducing Effect of Allium atroviolaceum Bulb Extract on Breast, Cervical, and Liver Cancer Cells, Front Pharmacol, 8 (2017) 5. https://doi.org/10.3389/fphar.2017.00005.
[55] P.G. Cadena, M.A. Pereira, R.B.S. Cordeiro, I.M.F. Cavalcanti, B. Barros Neto, M.d.C.C.B. Pimentel, J.L. Lima Filho, V.L. Silva, N.S. Santos-Magalhães, Nanoencapsulation of quercetin and resveratrol into elastic liposomes, Biochimica et Biophysica Acta (BBA) - Biomembranes, 1828 (2013) 309-316. https://doi.org/10.1016/j.bbamem.2012.10.022.
[56] N. Graham, C.-c. Jiang, X.-Z. Li, J.-Q. Jiang, J. Ma, The influence of pH on the degradation of phenol and chlorophenols by potassium ferrate, Chemosphere, 56 (2004) 949-956. https://doi.org/10.1016/j.chemosphere.2004.04.060.
[57] P. Trucillo, R. Campardelli, E. Reverchon, Liposomes: From Bangham to Supercritical Fluids, Processes, 8 (2020). https://doi.org/10.3390/pr8091022.

[58] Y.P. Patil, S. Jadhav, Novel methods for liposome preparation, Chemistry and Physics of Lipids, 177 (2014) 8-18. https://doi.org/10.1016/j.chemphyslip.2013.10.011.
[59] A. Pawar, C. Bothiraja, K. Shaikh, A. Mali, An insight into cochleates, a potential drug delivery system, RSC Advances, 5 (2015) 81188-81202. https://doi.org/10.1039/C5RA08550K.
[60] N.B.M. Ağardan, Z. Değim, Ş. Yılmaz, L. Altıntaş, T. Topal, The Effectiveness of Raloxifene-Loaded Liposomes and Cochleates in Breast Cancer Therapy, AAPS PharmSciTech, 17 (2016) 968-977. https://doi.org/10.1208/s12249-015-0429-3.
[61] Shuddhodana, Z. Judeh, Alginate-coating of artemisinin-loaded cochleates results in better control over gastro-intestinal release for effective oral delivery, Journal of Drug Delivery Science and Technology, 52 (2019) 27-36. https://doi.org/10.1016/j.jddst.2019.04.020.
[62] E.H. Gokce, E. Korkmaz, E. Dellera, G. Sandri, M.C. Bonferoni, O. Ozer, Resveratrol-loaded solid lipid nanoparticles versus nanostructured lipid carriers: evaluation of antioxidant potential for dermal applications, Int J Nanomedicine, 7 (2012) 1841-1850. https://doi.org/10.2147/IJN.S29710.
[63] S. Jagwani, S. Jalalpure, D. Dhamecha, K. Jadhav, R. Bohara, Pharmacokinetic and Pharmacodynamic Evaluation of Resveratrol Loaded Cationic Liposomes for Targeting Hepatocellular Carcinoma, ACS Biomaterials Science & Engineering, 6 (2020) 4969-4984. https://doi.org/10.1021/acsbiomaterials.0c00429.
[64] S. Jose, S.S. Anju, T.A. Cinu, N.A. Aleykutty, S. Thomas, E.B. Souto, In vivo pharmacokinetics and biodistribution of resveratrol-loaded solid lipid nanoparticles for brain delivery, International Journal of Pharmaceutics, 474 (2014) 6-13. https://doi.org/10.1016/j.ijpharm.2014.08.003.
[65] S. Wan, L. Zhang, Y. Quan, K. Wei, Resveratrol-loaded PLGA nanoparticles: enhanced stability, solubility and bioactivity of resveratrol for non-alcoholic fatty liver disease therapy, Royal Society Open Science, 5 (2018) 181457. https://doi.org/10.1098/rsos.181457.
[66] R.J. Mannino, S. Gould-Fogerite, S.L. Krause-Elsmore, D. Delmarre, R. Lu, Encochleation methods, cochleates and methods of use, U.S. Patent 9,974,745, (2018).
[67] J.K. Patra, G. Das, L.F. Fraceto, E.V.R. Campos, M.d.P. Rodriguez-Torres, L.S. Acosta-Torres, L.A. Diaz-Torres, R. Grillo, M.K. Swamy, S. Sharma, S. Habtemariam, H.-S. Shin, Nano based drug delivery systems: recent developments and future prospects, Journal of Nanobiotechnology, 16 (2018) 71. https://doi.org/10.1186/s12951-018-0392-8.

[68] G.P. Panotopoulos, Z.S. Haidar, Mathematical Modeling for Pharmaco-Kinetic and -Dynamic Predictions from Controlled Drug Release NanoSystems: A Comparative Parametric Study, Scientifica, 2019 (2019) 9153876. https://doi.org/10.1155/2019/9153876.
[69] S.N. Pinto, L.C. Silva, R.F.M. de Almeida, M. Prieto, Membrane Domain Formation, Interdigitation, and Morphological Alterations Induced by the Very Long Chain Asymmetric C24:1 Ceramide, Biophysical Journal, 95 (2008) 2867-2879. https://doi.org/10.1529/biophysj.108.129858.
[70] M. Lopes, N. Shrestha, A. Correia, M.-A. Shahbazi, B. Sarmento, J. Hirvonen, F. Veiga, R. Seiça, A. Ribeiro, H.A. Santos, Dual chitosan/albumin-coated alginate/dextran sulfate nanoparticles for enhanced oral delivery of insulin, Journal of Controlled Release, 232 (2016) 29-41. https://doi.org/10.1016/j.jconrel.2016.04.012.
[71] X. Zhong, B. Chen, Z. Yang, Nanocochleates as the Potential Delivery Systems for Oral Antitumor of Hydroxycamptothecin, Journal of Biomedical Nanotechnology, 14 (2018) 1339-1346. https://doi.org/10.1166/jbn.2018.2572.
[72] S.K. Lai, Y.-Y. Wang, D. Wirtz, J. Hanes, Micro- and macrorheology of mucus, Advanced Drug Delivery Reviews, 61 (2009) 86-100. https://doi.org/10.1016/j.addr.2008.09.012.
[73] K. Gradauer, J. Barthelmes, C. Vonach, G. Almer, H. Mangge, B. Teubl, E. Roblegg, S. Dünnhaupt, E. Fröhlich, A. Bernkop-Schnürch, R. Prassl, Liposomes coated with thiolated chitosan enhance oral peptide delivery to rats, Journal of Controlled Release, 172 (2013) 872-878. https://doi.org/10.1016/j.jconrel.2013.10.011.
[74] R.R. Bhosale, H.V. Gangadharappa, D.V. Gowda, R.A.M. Osmani, R. Vaghela, A Review on Nanocochleates: The Inimitable Nanoparticulate Drug Carriers, Advanced Science, Engineering and Medicine, 9 (2017) 359-369. https://doi.org/10.1166/asem.2017.2020.
[75] U.M. Syed, A.F. Woo, F. Plakogiannis, T. Jin, H. Zhu, Cochleates bridged by drug molecules, International Journal of Pharmaceutics, 363 (2008) 118-125. https://doi.org/10.1016/j.ijpharm.2008.06.026.
[76] R.J. Ahiwale, B. Chellampillai, A.P. Pawar, Investigation of novel sorafenib tosylate loaded biomaterial based nano-cochleates dispersion system for treatment of hepatocellular carcinoma, Journal of Dispersion Science and Technology, (2021) 1-19. https://doi.org/10.1080/01932691.2021.1878034.
[77] V. Leonhard, R.V. Alasino, I.D. Bianco, A.G. Garro, V. Heredia, D.M. Beltramo, Self-assembled micelles of monosialogangliosides as nanodelivery vehicles for taxanes, Journal of Controlled Release, 162 (2012) 619-627. https://doi.org/10.1016/j.jconrel.2012.07.031.

[78] R. Chai, H. Fu, Z. Zheng, T. Liu, S. Ji, G. Li, Resveratrol inhibits proliferation and migration through SIRT1 mediated post-translational modification of PI3K/AKT signaling in hepatocellular carcinoma cells, Mol Med Rep, 16 (2017) 8037-8044. https://doi.org/10.3892/mmr.2017.7612.
[79] D. Colin, A. Lancon, D. Delmas, G. Lizard, J. Abrossinow, E. Kahn, B. Jannin, N. Latruffe, Antiproliferative activities of resveratrol and related compounds in human hepatocyte derived HepG2 cells are associated with biochemical cell disturbance revealed by fluorescence analyses, Biochimie, 90 (2008) 1674-1684. https://doi.org/10.1016/j.biochi.2008.06.006.
[80] L. Zarif, D. Perlin, Amphotericin B nanocochleates: from formulation to oral efficacy, Drug Delivery Technology, 2 (2002) 34-37.
[81] S.H. Kim, B.B. Adhikari, S. Cruz, M.P. Schramm, J.A. Vinson, V. Narayanaswami, Targeted Intracellular Delivery of Resveratrol to Glioblastoma Cells Using Apolipoprotein E-Containing Reconstituted HDL as a Nanovehicle, PLOS ONE, 10 (2015) e0135130. https://doi.org/10.1371/journal.pone.0135130.
[82] R.S.Y. Wong, Apoptosis in cancer: from pathogenesis to treatment, Journal of Experimental & Clinical Cancer Research, 30 (2011) 87. https://doi.org/10.1186/1756-9966-30-87.
[83] M. Massimi, A. Tomassini, F. Sciubba, A.P. Sobolev, L.C. Devirgiliis, A. Miccheli, Effects of resveratrol on HepG2 cells as revealed by 1H-NMR based metabolic profiling, Biochimica et Biophysica Acta (BBA) - General Subjects, 1820 (2012) 1-8. https://doi.org/10.1016/j.bbagen.2011.10.005.
[84] S. Verma, A. Bhardwaj, M. Vij, P. Bajpai, N. Goutam, L. Kumar, Oleic acid vesicles: a new approach for topical delivery of antifungal agent, Artificial Cells, Nanomedicine, and Biotechnology, 42 (2014) 95-101. https://doi.org/10.3109/21691401.2013.794351.
[85] W. Zhang, Y. Sui, J. Ni, T. Yang, Insights into the Nanog gene: A propeller for stemness in primitive stem cells, Int J Biol Sci, 12 (2016) 1372-1381. https://doi.org/10.7150/ijbs.16349.
[86] A. Sato, M. Okada, K. Shibuya, E. Watanabe, S. Seino, K. Suzuki, Y. Narita, S. Shibui, T. Kayama, C. Kitanaka, Resveratrol promotes proteasome-dependent degradation of Nanog via p53 activation and induces differentiation of glioma stem cells, Stem Cell Research, 11 (2013) 601-610. https://doi.org/10.1016/j.scr.2013.04.004.
[87] F.-W. Hu, L.-L. Tsai, C.-H. Yu, P.-N. Chen, M.-Y. Chou, C.-C. Yu, Impairment of tumor-initiating stem-like property and reversal of epithelial–mesenchymal transdifferentiation in head and neck cancer by resveratrol treatment, Molecular Nutrition & Food Research, 56 (2012) 1247-1258. https://doi.org/10.1002/mnfr.201200150.

[88] S. Shankar, D. Nall, S.-N. Tang, D. Meeker, J. Passarini, J. Sharma, R.K. Srivastava, Resveratrol Inhibits Pancreatic Cancer Stem Cell Characteristics in Human and KrasG12D Transgenic Mice by Inhibiting Pluripotency Maintaining Factors and Epithelial-Mesenchymal Transition, PLOS ONE, 6 (2011) e16530. https://doi.org/10.1371/journal.pone.0016530.

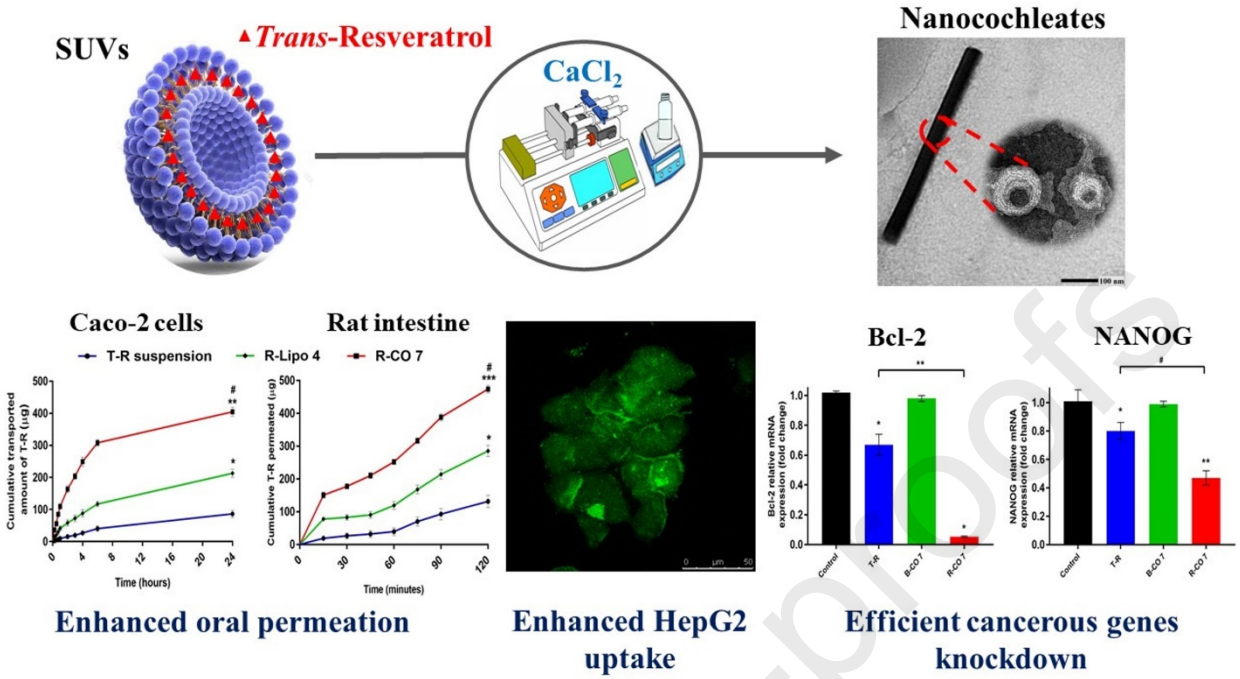

Highlights

- *Trans*-Resveratrol-loaded nanocochleates were prepared by trapping method
- Monodisperse nano-sized cylinders with high Resveratrol encochleation
- Controlled release pattern and stable lyophilized powder were accomplished
- Significant enhancement of oral permeation via Caco-2 and rat intestinal models
- Boosted cytotoxicity, high cellular uptake and augmented apoptosis in HepG2 cells

Figure Captions

Fig. 1. *In-vitro* stability of saturated solutions of T-R at different pH levels (pH 5.5, pH 6.8 and pH 7.4) for 72 h at 37 ℃. Data are expressed as mean ± SD, (n = 3). Statistical comparison of the overall trend (using unpaired Student's t-test) among different buffers over 3 days was significant (# $p \leq 0.05$ *vs.* pH 6.8 and * $p \leq 0.01$ *vs.* pH 7.4).

Fig. 2. Morphological examination of T-R-loaded nanocarriers. (I) SEM images of (a) R-Lipo 4 and (b) R-CO 7 dispersions; scale bars 500 nm. (II) TEM images of (c-d) R-CO 7 dispersion; scale bars 100 nm. Yellow arrows point to snail-like, rolling structure of nanocochleates.

Fig. 3. Solid-state characteristics of T-R-loaded nanocarriers. (I) DSC thermograms and (II) FTIR spectra of (a) T-R, (b) R-Lipo 4 physical mixture, (c) R-Lipo 4 formula, (d) R-CO 7 physical mixture and (e) R-CO 7 formula along with FTIR spectra of soybean PC (Lipoid® S75) and cholesterol.

Fig. 4. *In-vitro* release profile of T-R from drug suspension (in acetate buffer, pH 5.5), R-Lipo 4 and R-CO 7 in phosphate-buffered saline (pH 6.8) at 100 rpm and 37 °C using dialysis bag method. Data are expressed as mean ± SD, (n = 3).

Fig. 5. Shelf-stability study of T-R-loaded nanocarriers. (I) Average particle size of reconstituted R-Lipo 4 and R-CO 7 lyophilized powders after 6 months of storage at 25±2℃ and < 5% RH. Data are expressed as mean ± SD, (n = 3). Statistical difference was significant (# $p \leq 0.0001$) *vs.* zero-time using one-way ANOVA test followed by Tukey's test. (II) TEM images of (a) R-Lipo 4 and (c) R-CO 7 dispersions at zero-time compared with reconstituted lyophilized powders of (b) R-Lipo 4 and (d) R-CO 7 after 6 months of storage at 25±2℃ and < 5% RH. Scale bars 500 nm (a), 1 µm (b) and 100 nm (c-d). Yellow arrows indicate spiral rolling structure of nanocochleates.

Fig. 6. Permeation studies of T-R-loaded nanocarriers. (I) Caco-2 cells cultured on the apical compartment of the Transwell® inserts forming a monolayer shown by the nuclear fluorescent Hoechst 33342 stain (blue fluorescence) visualized under confocal laser scanning microscope (CLSM) (a) on 9th day of post-seeding and (b) at the end of the experiment; 21 days. Yellow double-head arrows indicate intercellular gaps among Caco-2 nuclei. (II) Transport profiles of T-R suspension, R-Lipo 4 and R-CO 7 across Caco-2 cell monolayer. (III) *Ex-vivo* permeation of T-R through non-everted rat intestine from T-R suspension (in acetate buffer, pH 5.5), R-Lipo 4

and R-CO 7. Data are expressed as mean ± SD, (n = 3). Statistical differences were significant (* $p \leq 0.05$, ** $p \leq 0.01$, *** $p \leq 0.001$ *vs.* T-R suspension and # $p \leq 0.05$ *vs.* R-Lipo 4).

Fig. 7. (I) *In-vitro* cytotoxicity studies of T-R-loaded nanocarriers on HepG2 cell line. Cells were treated with serial concentrations of T-R, R-Lipo 4, R-CO 7 and their respective blank formulations equivalent to [2.5-200] µM for 24 h (a) and 48 h (b). Cell viability was measured by MTT assay. Data are expressed as mean ± SD, (n = 3). Black extrapolated dotted lines correspond to the IC_{50} values. (II) Confocal laser scanning microscope (CLSM) images showing cellular uptake of R-Lipo 4 and R-CO 7 formulations in HepG2 cells after 1h incubation with the 24 h IC_{50} values of each test samples. Green fluorescence of nanocarriers (T-R) and blue fluorescence of nucleus (Hoechst 33342). Scale bar 25 µm.

Fig. 8. HepG2 cellular uptake of T-R and loaded formulations. (I) CLSM images showing cellular uptake of free T-R, R-Lipo 4 and R-CO 7 in HepG2 cells. For all treatment groups, cells were 1 h-treated with the IC_{50} (24 h-treatment) of free T-R. Scale bar 50 µm. 3D surface plots of each image were drawn using Image J software (version-1.52a). (II) Quantification of mean fluorescence intensity by analysis of CLSM images of cellular uptake using Image J software. Data are presented as mean ± SD, (n = 3). Statistical differences were significant (* $p \leq 0.05$, ** $p \leq 0.0001$) *vs.* T-R and (# $p \leq 0.0001$).

Fig. 9. Apoptotic effect of T-R and loaded formulations in HepG2 cells. (I) CLSM images showing HepG2 nuclei labelled with Hoechst 33342 dye (blue fluorescence) after 24 h-treatment with T-R, R-Lipo 4, R-CO 7 and their respective blank counterparts (B-Lipo, B-CO 7) at the equivalent 24 h IC_{50} of T-R in comparison with the control untreated cells. Lower panel of microphotographs represents merged matched fields between upper panel of Hoechst staining and phase contrast images. Scale bars 25 µm (control, B-Lipo, B-CO 7) and 50 µm (T-R, R-Lipo 4, R-CO 7). White arrows point to the nuclear fragmentation and apoptotic bodies. (II) Percentage of apoptosis index (AI) in HepG2 cells after 24 h-treatment with the equivalent 24 h IC_{50} of T-R in the above-mentioned groups. Statistical differences were significant (*, ** and # $p \leq 0.0001$) *vs.* control, T-R and R-Lipo 4, respectively.

Fig. 10. Knockdown of anti-apoptotic (Bcl-2) and cancer stemness (NANOG) biomarker genes in HepG2 cells. Expression level of (I) Bcl-2 and (II) NANOG genes in HepG2 cells after treatment with the 24 h IC_{50} of T-R for 24 h using T-R, R-CO 7 and its blank counterpart compared to control untreated cells. Bcl-2 and NANOG expressions were normalized against GAPDH levels. All data are expressed as mean ± SD, (n = 3). Statistical differences were significant (I); (* $p \leq 0.0001$ *vs.* control) and (** $p \leq 0.0001$) while (II); (* $p \leq 0.05$, ** $p \leq 0.0001$ *vs.* control) and (# $p \leq 0.001$).

Table 1. Forward (F) and reverse (R) primers used for qRT-PCR analysis including sequences, size and melting temperature.

Gene	Primer	Sequence of nucleotides (nt)	T_m (℃)	Size (nt)	Product length (bp)
NANOG	F	5'-GGAAGACAAGGTCCCGGTCAA-3'	59.2	21	166
	R	5'-CCAGGTCTTCACCTGTTTGTAGC-3'	57.8	23	
Bcl-2	F	5'-CTTTGAGTTCGGTGGGGTCA-3'	57.3	20	162
	R	5'-GGGCCGTACAGTTCCACAAA-3'	57.8	20	
GAPDH	F	5'-TCCTGCACCACCAACTGCTTAG-3'	59.5	22	90
	R	5'-GGCATGGACTGTGGTCATGAGT-3'	59.4	22	

Abbreviations: qRT-PCR, quantitative real-time polymerase chain reaction; T_m, melting temperature; bp, base pair.

Table 2. Effect of preparation methods of different T-R-loaded nanocarriers; liposomes (R-Lipo) and nanocochleates (R-CO) on particle attributes; mean particle size, polydispersity index (PDI), zeta potential (ZP), entrapment efficiency (EE), drug loading and product yield. Results are expressed as mean ± SD, (n = 3).

Formula code	Method of preparation	Final [$CaCl_2$] (mM)	Average particle size (nm)	PDI	ζ-potential (mV)	Entrapment efficiency (EE %)	Drug loading (mg/g)	Yield (%)
R-Lipo 1	Thin film hydration	-------	188.95 ±1.48	0.209± 0.02	-54.25± 1.39	93.16±0 .82	46.62± 0.41	75.29± 1.2
R-CO 2		9	225.76 ±6.12	0.298± 0.024	-50.92± 1.47	95.08±1 .51	45.18± 0.74	78.32± 1.43
R-CO 3		16.67	259.45 ±4.73	0.367± 0.016	-43.17± 1.28	96.81±0 .39	44.01± 0.23	80.11± 2.63
R-Lipo 4	Ethanol injection	-------	120.18 ±1.07	0.113± 0.005	-61.31± 2.34	97.74±0 .23	48.9±0 .12	93.61± 0.45
R-CO 5		6	126.56 ±0.89	0.164± 0.01	-57.29± 2.66	98.06±0 .09	47.32± 0.01	95.33± 1.58

R-CO 6	9	140.23 ±2.72	0.201± 0.007	-54.13± 2.14	98.42±0 .2	46.76± 0.15	96.59± 0.37
R-CO 7	16.67	163.27 ±2.68	0.25±0. 011	-46.62± 1.12	99.69±0 .12	45.31± 0.14	98.13± 1.54
R-CO 8	26	295.67 ±5.42	0.482± 0.014	-32.19± 0.86	99.75±0 .05	43.16± 0.01	98.09± 1.72

Abbreviations: SD, standard deviation; [$CaCl_2$], concentration of calcium chloride; PDI, polydispersity index.

Table 3. Fitting *in-vitro* release data of T-R suspension, R-Lipo 4 and R-CO 7 to different release kinetic models.

	Kinetic model		
	First-order	**Higuchi**	**Korsmeyer-Peppas**

Samples	Fitting equation [$\ln(1-F/100) = -k_1*t$]	R^2	Fitting equation [$F=k_H*t^{0.5}$]	R^2	Fitting equation [$F=k_{KP}*t^n$]	R^2	n
T-R suspension	$\ln(1- F/100) = -0.019*t$	0.9204	$F=8.076*t^{0.5}$	0.9952	$F=7.983*t^{0.5}$	0.9946	0.5
R-Lipo 4	$\ln(1- F/100) = -0.204*t$	0.9691	$F=15.022*t^{0.5}$	0.6929	$F=32.545*t^{0.29}$	0.9363	0.29
R-CO 7	$\ln(1- F/100) = -0.067*t$	0.9658	$F=12.776*t^{0.5}$	0.9827	$F=16.059*t^{0.44}$	0.9869	0.44

Table 4. Apparent permeability coefficient (P_{app}) values from Caco-2 transport and *ex-vivo* intestinal permeation studies along with TEER values of Caco-2 monolayers before and after the transport study. Results are expressed as mean ± SD, (n = 3).

Samples	Caco-2 permeation			*Ex-vivo* permeation
	P_{app} ($\times 10^{-6}$cm/s)	TEER (Ω.cm^2)		P_{app} ($\times 10^{-8}$cm/s)
		Initial	Final	
T-R suspension	1.69±0.11	787±10.25	751±9.43	1.92±0.17
R-Lipo 4	3.86±0.27	768±13.64	746±7.18	3.62±0.24
R-CO 7	6.8±0.88	795±9.11	778±6.24	6.67±0.23

Abbreviations: SD, standard deviation; TEER, transepithelial electrical resistance; s, second.

Figure

Click here to access/download;Figure;Figures.docx

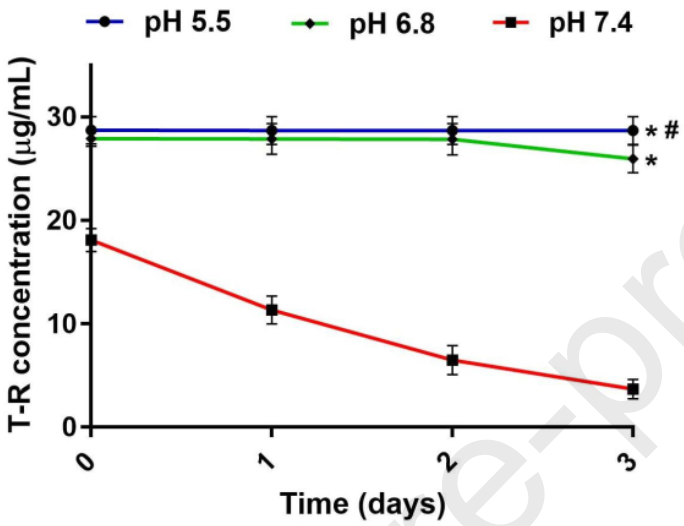

Fig. 1. *In-vitro* stability of saturated solutions of T-R at different pH levels (pH 5.5, pH 6.8 and pH 7.4) for 72 h at 37 ℃. Data are expressed as mean ± SD, (n = 3). Statistical comparison of the overall trend (using unpaired Student's t-test) among different buffers over 3 days was significant (# $p \leq 0.05$ *vs.* pH 6.8 and * $p \leq 0.01$ *vs.* pH 7.4).

(Single fitting image)

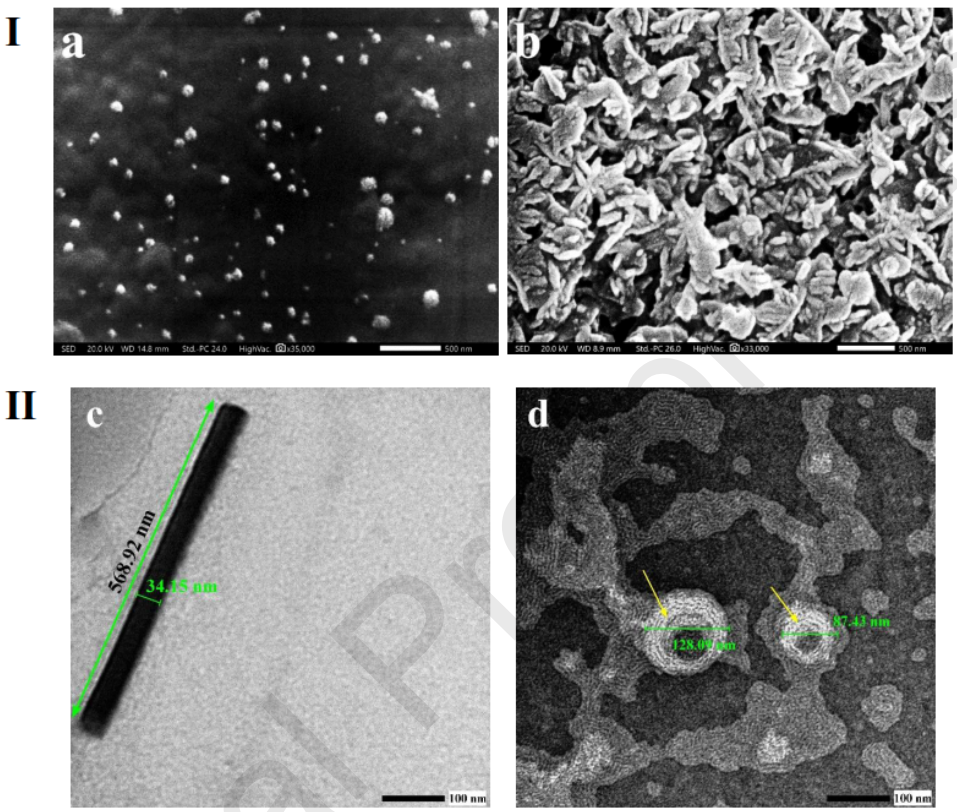

Fig. 2. Morphological examination of T-R-loaded nanocarriers. (I) SEM images of (a) R-Lipo 4 and (b) R-CO 7 dispersions; scale bars 500 nm. (II) TEM images of (c-d) R-CO 7 dispersion; scale bars 100 nm. Yellow arrows point to snail-like, rolling structure of nanocochleates.

(Single fitting image)

I

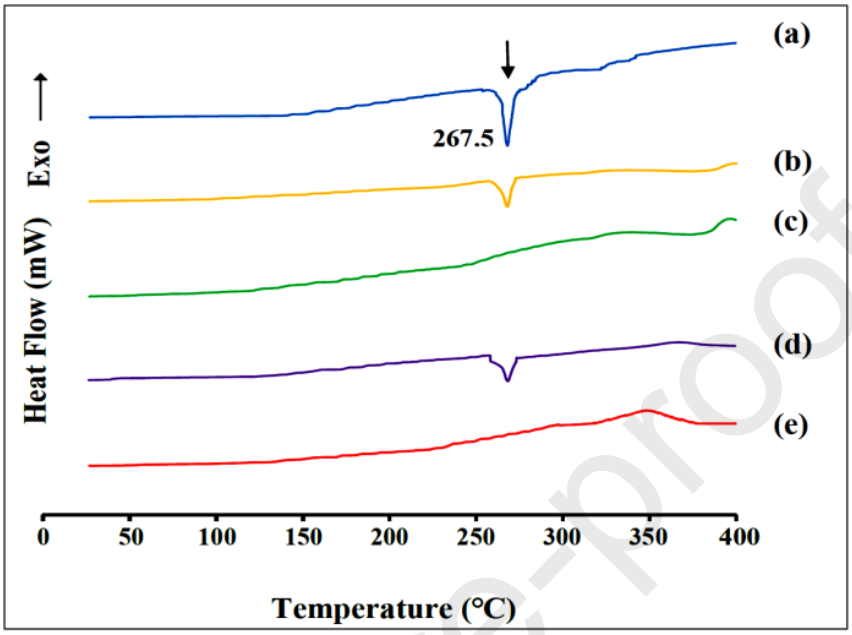

II

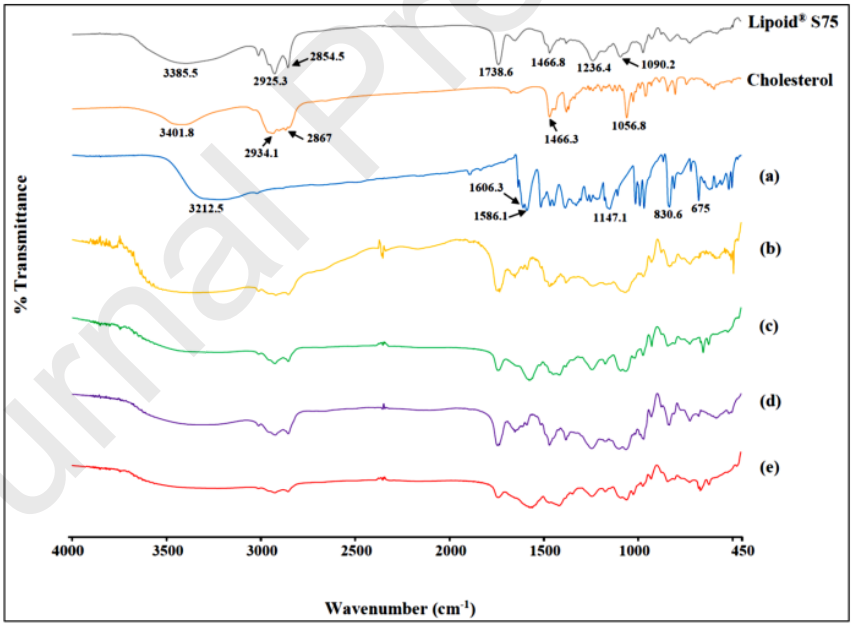

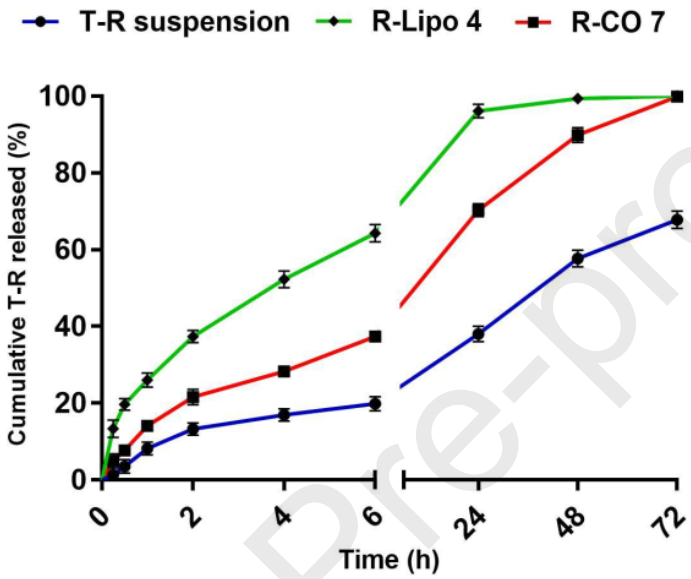

Fig. 4. *In-vitro* release profile of T-R from drug suspension (in acetate buffer, pH 5.5), R-Lipo 4 and R-CO 7 in phosphate-buffered saline (pH 6.8) at 100 rpm and 37 °C using dialysis bag method. Data are expressed as mean ± SD, (n = 3).

(Single fitting image)

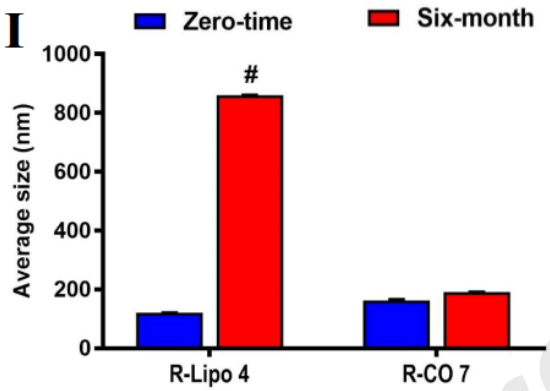
I
Zero-time
Six-month
1000
800
600
400
200
0
Average size (nm)
#
R-Lipo 4
R-CO 7

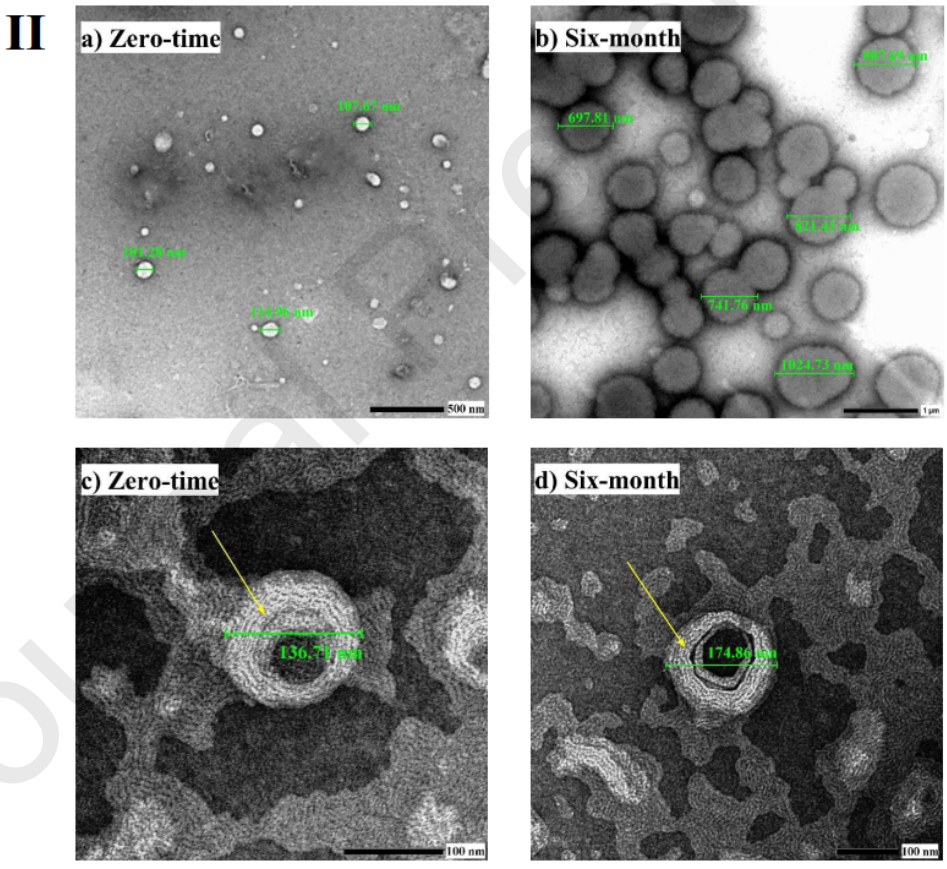
II
a) Zero-time
b) Six-month
697.81 nm
500 nm
1 µm
c) Zero-time
136.71 nm
d) Six-month
174.86 nm
100 nm
100 nm

6

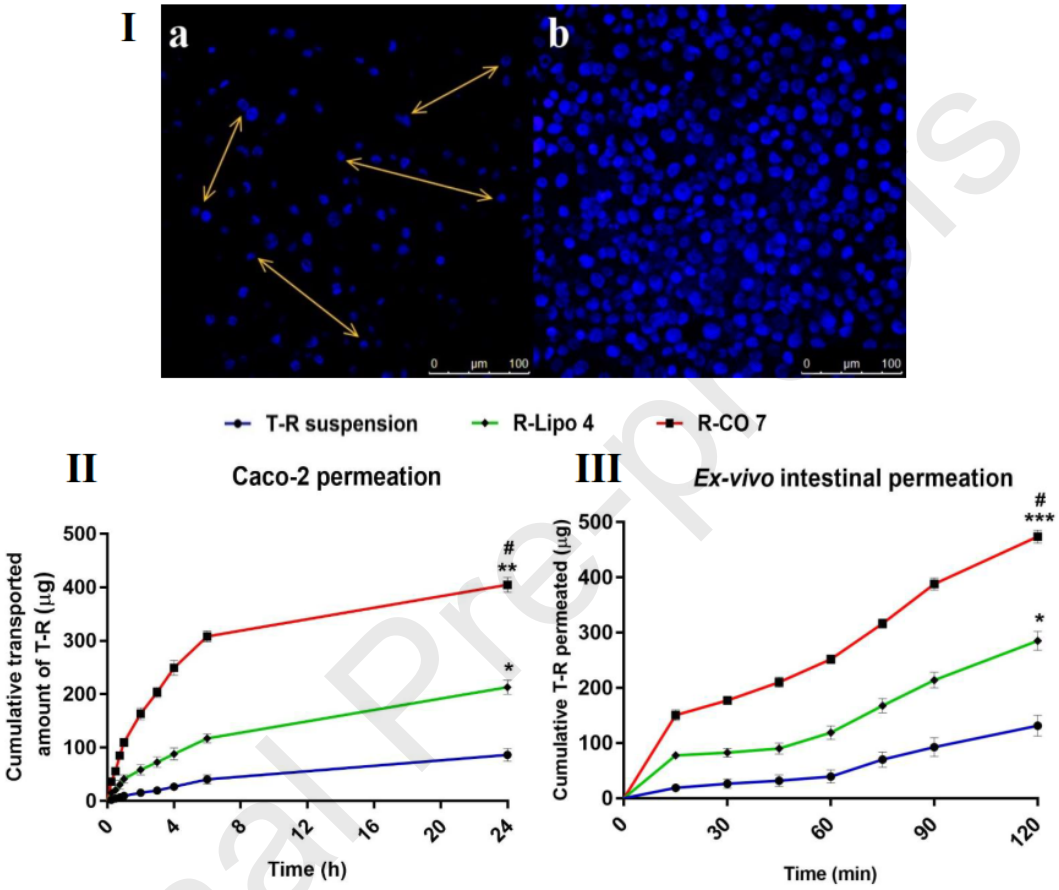

Fig. 6. Permeation studies of T-R-loaded nanocarriers. (I) Caco-2 cells cultured on the apical compartment of the Transwell® inserts forming a monolayer shown by the nuclear fluorescent Hoechst 33342 stain (blue fluorescence) visualized under confocal laser scanning microscope (CLSM) (a) on 9th day of post-seeding and (b) at the end of the experiment; 21 days. Yellow double-head arrows indicate intercellular gaps among Caco-2 nuclei. (II) Transport profiles of T-R suspension, R-Lipo 4 and R-CO 7 across Caco-2 cell monolayer. (III) *Ex-vivo* permeation of T-R through non-everted rat intestine from T-R suspension (in acetate buffer, pH 5.5), R-Lipo 4 and R-CO 7. Data are expressed as mean ± SD, (n = 3). Statistical differences were significant (* $p \leq 0.05$, ** $p \leq 0.01$, *** $p \leq 0.001$ *vs.* T-R suspension and # $p \leq 0.05$ *vs.* R-Lipo 4).

(2 Column-fitting image)

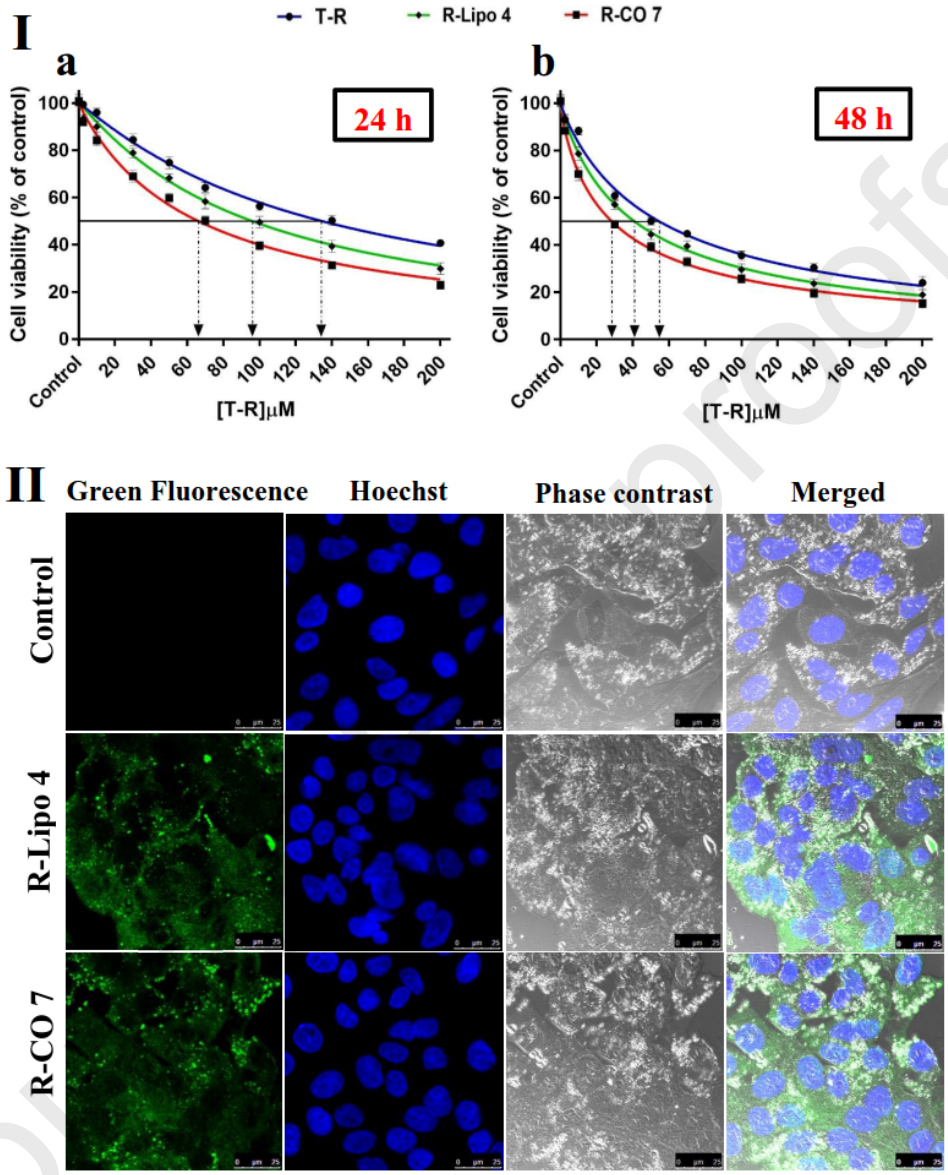

Fig. 7. (I) *In-vitro* cytotoxicity studies of T-R-loaded nanocarriers on HepG2 cell line. Cells were treated with serial concentrations of T-R, R-Lipo 4, R-CO 7 and their respective blank formulations equivalent to [2.5-200] µM for 24 h (a) and 48 h (b). Cell viability was measured by MTT assay. Data are expressed as mean ± SD, (n = 3). Black extrapolated dotted lines

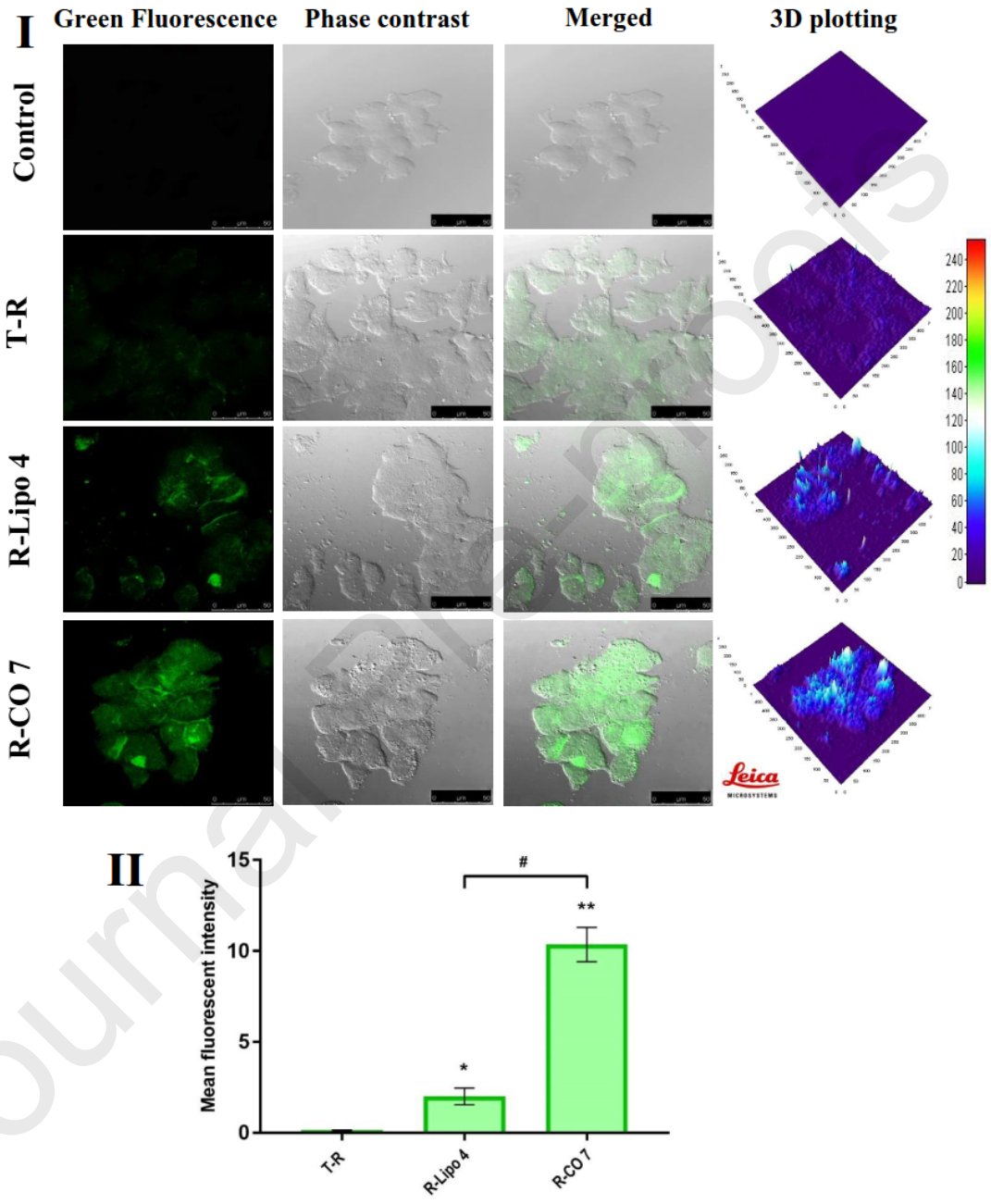
I
Green Fluorescence
Phase contrast
Merged
3D plotting
Control
T-R
R-Lipo 4
R-CO 7
240
220
200
180
160
140
120
100
80
60
40
20
0
Leica
MICROSYSTEMS
II
Mean fluorescent intensity
15
10
5
0
#
**
*
T-R
R-Lipo 4
R-CO 7

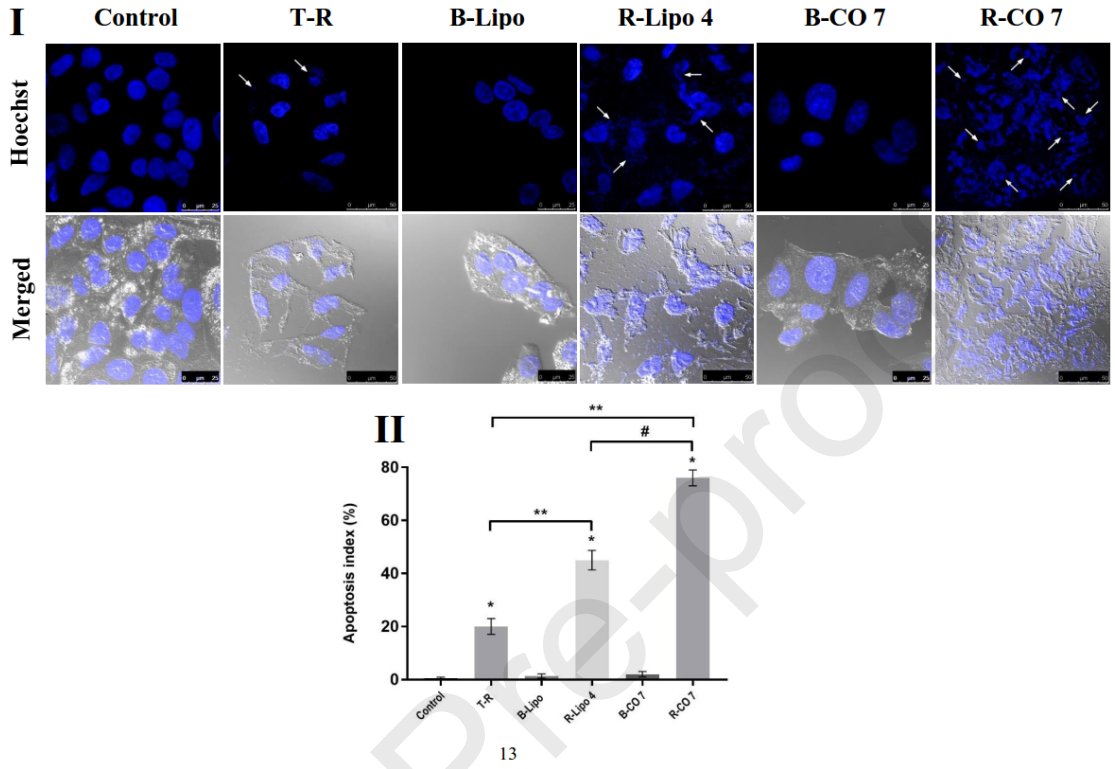

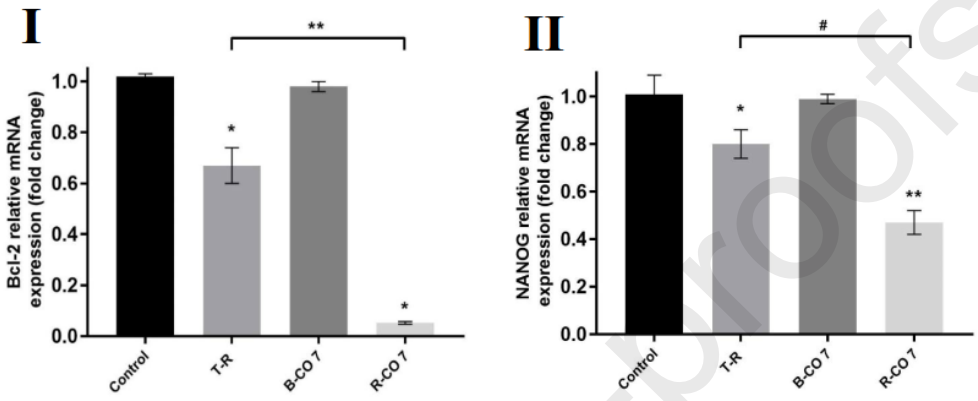

Fig. 10. Knockdown of anti-apoptotic (Bcl-2) and cancer stemness (NANOG) biomarker genes in HepG2 cells. Expression level of (I) Bcl-2 and (II) NANOG genes in HepG2 cells after treatment with the 24 h IC_{50} of T-R for 24 h using T-R, R-CO 7 and its blank counterpart compared to control untreated cells. Bcl-2 and NANOG expressions were normalized against GAPDH levels. All data are expressed as mean ± SD, (n = 3). Statistical differences were significant (I); (* $p \leq 0.0001$ *vs.* control) and (** $p \leq 0.0001$) while (II); (* $p \leq 0.05$, ** $p \leq 0.0001$ *vs.* control) and (# $p \leq 0.001$).

(2 Column-fitting image)